Applied Energy 391 (2025) 125844

Contents lists available at ScienceDirect

Applied Energy

journal homepage: www.elsevier.com/locate/apenergy

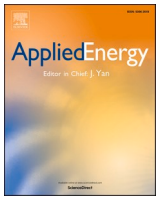

Enhancing solar tower competitiveness with star-shaped receivers

Giancarlo Gentile [a,*], Francesco Stefano Carli [a], Matteo Speranzella [a], Marco Binotti [a], Michael E. Cholette [b], Giampaolo Manzolini [a]

[a] Politecnico di Milano, Department of Energy, via Lambruschini 4A, 20156, Milan, Italy
[b] Queensland University of Technology, Science and Engineering Faculty, 2 George St, 4000 Brisbane, QLD, Australia

HIGHLIGHTS

- Star-shaped receivers for solar tower plants are comprehensively analyzed.
- Three materials are compared for star receiver tubes: 740H, H230, and 800H.
- Thermomechanical performance and costs are compared to external receivers.
- For a Gemasolar-like solar field, the star receiver leads to 10 % LCOH reduction.
- Optimized solar field and star receiver leads to 75 % lower CAPEX and 30 % lower LCOH.

ARTICLE INFO

Keywords:
Star receiver
Solar tower
Optimization
Concentrated solar power
Creep-fatigue

ABSTRACT

Star-shaped receivers represent a novel receiver concept to increase performance and reduce cost of solar tower plants, boosting the competitiveness of these renewable and dispatchable power production technology. This article presents a comprehensive analysis of star-shaped receivers, which, due to their unique geometry, provide lower optical and thermal losses, increased lifetime, and reduced construction and maintenance costs. The article describes methodologies for assessing optical and thermal performance, pressure drop, creep-fatigue lifetime, wind load, and capital and operating costs of star receivers. Specifically, optical analysis is performed using ray-tracing simulation tools while tailored numerical models are implemented in MATLAB to investigate thermal, mechanical and economic aspects. The proposed methods allow to estimate the maximum receiver size that can withstand wind loads for a given location and optimize the design of this innovative receiver through a constrained parametric procedure based on Levelized Costs of Heat (LCOH) minimization. Results show that the cost of the star receiver can be up to 75 % cheaper than the corresponding Gemasolar-like cylindrical receiver with the same design thermal power. This cost reduction results from the adoption of fewer number of tubes and less expensive material as 800H instead of H230. Overall, the optimal plant configuration has a higher thermal energy collected by around 5 % annually, resulting in a 30 % reduction in LCOH with respect to Gemasolar-like cylindrical receiver case.

1. Introduction

Unlike intermittent renewable power plants such as photovoltaic and wind, Concentrated Solar Power (CSP) and integrated with Thermal Energy Storage enables renewable energy production in a dispatchable and flexible manner [1,2]. This makes CSP a promising technology, especially in regions with high renewable energy penetration which experience curtailment or low energy prices during peak renewable production hours [2]. Solar Tower (ST) is the CSP technology with higher cost reduction potential [3] and one solution to make this technology more competitive with other renewable systems is to enhance performance and reduce costs associated with the receiver, that is a key component of ST plants. Indeed, the receiver cost represents roughly 15 % of total plant capital cost [4] and 20–40 % of the energy incident on the receiver is lost due to thermal losses [5]. External cylindrical receivers represent the state-of-the-art for solar tower systems. Such receivers have one main inherent disadvantage: because the tubes are radiated from only one side, they operate with substantial temperature differences along the circumference that generate significant thermal

* Corresponding author.
E-mail address: giancarlo1.gentile@polimi.it (G. Gentile).

https://doi.org/10.1016/j.apenergy.2025.125844
Received 14 November 2024; Received in revised form 28 February 2025; Accepted 27 March 2025
Available online 13 April 2025

Nomenclature

Symbols

A	Area [m2]
c_{helio}	Heliostats specific cost [€/m2]
c_{land}	Land specific cost [€/m2]
c_{si}	Site specific improvement cost [€/m2]
C	Cost [€]
C_f	Force coefficient [−]
C_sC_d	Structural factor [−]
D	Diameter [m]
D_{tt}	Distance between adjacent tubes [m]
day_{eq}	Number of eq. days in one year [−]
f	Force per unit length [N/m]
F	Force [N] / View factor [−]
H	Height [m]
k	Factor for tubes mutual influence [−]
$\dot{m}$	Mass flow rate [kg/s]
N	Number [−]
$N_{d,y}$	Number of identical days per year [−]
N_p	Number of panels [−]
N_{tp}	Number of tubes per panel [−]
N_{tr}	Number of tubes per ray [−]
N_y	Number of years
p	Pressure [Pa]
Q	Thermal energy [Wh]
$\dot{Q}$	Thermal power [W]
R	Thermal resistance [W/m2K]
S_t	Pitch between adjacent tubes [m]
S_y	Yield strength [MPa]
t	Time [s]
th	Tube thickness [−]
T	Temperature [K]
T_{surr}	Equivalent Surrounding Temperature [K]
v	Velocity [m/s]
z	Axial coordinate [m]

Greek symbols

α_c	Tube coating absorptance [−]
Δp	Pressure drop [bar]
ε	Emissivity [−]
η	Efficiency [−]
ρ	Density [kg/m3]
ρ_{sup}	Support coating reflectivity [−]
σ_z	Axial stress [MPa]
σ_{UTS}	Ultimate Tensile Stress [MPa]

Acronyms

AR	Aspect Ratio
CAPEX	Capital EXpenditure
CSP	Concentrated Solar Power
HTF	Heat Transfer Fluid
KPI	Key Performance Indicator
LCOE	Levelized Cost Of Electricity
LCOH	Levelized Cost Of Heat
OPEX	Operating EXpenditure
PB	Power Block
SF	Solar Field
UTS	Ultimate Tensile Strength

Subscripts

amb	Ambient
adj	Adjacent
av	Average
conv	Convective
el	Electric
ext	External
i	Axial element
int	Internal
j	Circumferential element
max	Maximum
min	Minimum
next	Next circumferential volume
opt	Optical
out	Outlet
p	Panel
prev	Previous circumferential volume
rad	Radiative
rec	Receiver
rr	Ray-to-ray
stt	Solar-to-thermal
t	Tube
th	Thermal
tow	Tower
vol	Volume

Superscripts

des	Design
T	Thermal
y	Yearly

stresses. To prevent such stresses from leading to component failure, receivers need to be irradiated with limited thermal fluxes, the maximum value of which is generally considered to be 1 MW/m^2 in accordance with the main literature [6,7] and manufacturers' best practices [8]. Being able to irradiate the receiver with higher heat fluxes would allow to reduce its size, and thus thermal losses and cost, keeping the same thermal input. The most intuitive solution to achieve this is to act on the main cause of thermal stresses, namely asymmetric tube irradiation. In this context, star-shaped receivers, an innovative concept proposed by Sandia National Laboratories in 2014, represent a promising solution to overcome cylindrical receivers limitations, as they are designed to have tubes irradiated on both sides [9]. A three-dimensional representation of this receiver type, in its three-rays configuration, is shown in Fig. 1.

In addition to allowing the above-mentioned irradiation of tubes from both sides, the star-shaped receiver, compared with the conventional cylindrical one, has a number of other advantages: first is the reabsorption effect (also called light-trapping effect), by which the radiation reflected by tubes is redirected toward the other rays and absorbed by other tubes instead of being lost in the environment, hence

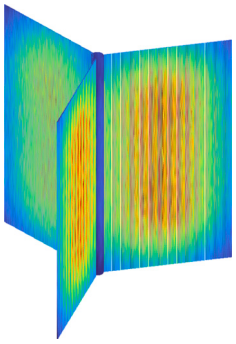

Fig. 1. Three rays star receiver 3D representation.

reducing reflective losses and increasing the effective solar absorptance. Second, view factors toward the environment are lower, thus reducing radiative losses. Third, with tubes being irradiated on both sides, tubes number can be halved maintaining the same irradiated surface, therefore significantly decreasing receiver cost compared to the cylindrical one.

The main drawback of the star configuration is related to the mechanical load due to the wind action on receiver structure: differently from a cylindrical receiver, which is back supported by the central tower providing stability and mechanical resistance, the star configuration exposes the entire surface to the environment without any back support.

In the 2014 study from Sandia National Laboratories [9], thermal performances of star receivers were investigated along with those of other fractal-like designs which take advantage of the light-trapping effect, at both meso (tubes shape) and macro (receiver geometry) scale. They showed how *meso*-scale finned geometries can improve the effective solar absorptance compared to flat surfaces, thanks to their capacity to trap the light. The impact was greater in case of materials with solar absorptance lower than 0.9. Such result, obtained through numerical models, was confirmed by experimental tests on corrugated samples of low absorptance material. They assessed how a star configuration can lead to lower radiative heat losses, due to reduced local view factors toward the environment. Furthermore, a greater concentration ratio can be obtained reducing the optical aperture, while maintaining the same exposed surface area and irradiance. At the macro scale a reduction of radiative heat losses up to 50 % and an improvement of thermal efficiency up to 10 % were achieved, considering SolarTwo cylindrical receiver as reference. However, they have not considered the reduction of the optical efficiency due to a smaller optical intercept area and the thermal analysis was performed in a simplified way, maintaining constant surface temperatures.

Such results were validated in further studies by Christian et al. [10,11] who analyzed three different configurations: vertical, horizontal and radially finned flat receivers. They proved how all the novel configurations have higher thermal efficiency compared to a flat plate receiver at same exposed surface, due to higher effective solar absorptance and lower radiative loss.

Puppe et al. [12] conducted a techno-economic analysis of different solar tower receivers, including a star receiver configuration. They claimed the star receiver achieved a 13 % lower LCOE compared to the reference solar tower, based on an upscaled version of Solar Two plant and with updated costs estimation. This result is due to the lower cost of tower and receiver, together with higher solar to electric efficiency. It is worth noticing that an LCOE reduction of 11.7 % was also achieved with an improved version of the reference case, which has higher solar to electric efficiency, lower receiver cost and lower self consumptions.

Wang et al. [13] investigated optical performances of five fin-like receivers, three with vertical fins and two with horizontal fins, while comparing them with a reference Gemasolar-like cylindrical receiver, keeping same solar field and same tubes size and number. The optical efficiency also includes reflective losses. They optimized each of the five receiver geometries, in terms of number of fins and internal support diameter and then selected the most performing one: a vertical finned receiver with six fins and small support, very similar to a star geometry. It achieves the highest optical efficiency equal to 63.9 %, 3.2 % higher than the cylindrical one. However, the heat flux is nonuniform, with an extremely high peak value equal to 3830 kW/m^2. This flux can be reduced by more than 40 % through the use of a multi-aiming point strategy, at the expense of the optical efficiency which slightly decreases.

Considering these results, a further study by Wang et al. [14] conducted a thermal analysis of a vertical finned receiver, whose performances were again compared with those of an external cylindrical receiver at fixed external diameter, assuming SolarTwo plant as a reference. First, the key geometric parameters of the fin-like receiver, including the fin number and inner diameter, are optimized with the unique constraint of the external diameter while the number of tubes can vary. The optimization was aimed at achieving the highest thermal efficiency without considering any additional cost related to a bigger receiver, since they affirmed that it accounts for a small percentage of the total cost and thus more tubes can be employed. The optimal configuration proved to be the one with an inner support diameter of 1 m and twelve fins (and almost double number of tubes), achieving a maximum thermal efficiency (including reflective losses) of 87.3 %, which is 3.7 % higher than that of the reference cylindrical receiver. This result is determined by a strong reduction of reflective losses while radiative and convective losses were instead higher due to the much larger exposed area. Compared to the previous study, the flux distribution is more uniform with a lower peak value: 442 kW/m^2 and 720 kW/m^2 for finned and cylindrical receiver respectively. The analysis was only based on thermal efficiency and the resulting optical efficiency was not reported, even though they stated that cylindrical receiver has a higher intercepted power due to lower spillage losses.

Binder et al. [15] investigated the lifetime of a three rays star receiver compared with that of a reference cylindrical receiver. Different cases were evaluated, varying wall thickness, mass flow rate and radiation intensity. This receiver arrangement halves the number of tubes compared to the reference cylindrical one, maintaining same exposed surface and approximately halving the cost. They designed the receiver with an inner supporting structure and pylons attached to the external side of the last tube of each ray, as well as with an upper roof and a proper tower connection. Additionally, three horizontal structures along receiver height are included, in order to withstand wind loads, which becomes more critical as the tubes diameter decreases. Results showed that double-sided irradiated tubes increase lifetime by a factor of 5–12 (depending on the load case) compared with one-sided irradiated tubes, thanks to the reduced temperature gradient between front and rear part of tubes. Thus, receiver cost can be further decreased by using a cheaper material with lower mechanical performances, preserving an acceptable lifetime. Alternatively, higher local flux densities can be reached at fixed material. Furthermore, they highlighted that particular attention should be paid to the aiming strategy, as front and back side of tubes should be irradiated as homogeneously as possible since a difference in radiation intensity will decrease tube's lifetime.

Different studies have been published demonstrating star receiver's potentialities, though concentrating on only one or few aspects. However, to the author's knowledge no studies have been published performing a comprehensive analysis of star receivers, assessing optical and thermal performances, receiver pressure drop, creep-fatigue lifetime, wind load impact and capital and operating costs. Moreover, no studies were found in literature comparing performance and cost of star-shaped receivers with those of state-of-the-art external cylindrical receivers to demonstrate, through the adoption of techno-economic KPI such as the Levelized Cost of Heat (LCOH), the advantages of this innovative configuration. This study aims at filling this literature gap, analyzing

with a comprehensive approach star receivers design and operation and achieving three main objectives: i) estimate the maximum receiver size that can withstand the wind load under typical operating conditions; ii) develop a methodology to optimize from a techno-economic point of view the design of a star receiver; iii) compare performance and costs of the star receiver with those of a conventional cylindrical one.

2. Methodology

The three objectives of this work are achieved through the following approach:

- the maximum receiver size that can withstand the wind load is evaluated through a simplified methodology described in Section 2.1, considering different tubes materials and diameters as well as different values of receiver aspect ratio (i.e., ratio between receiver height and external diameter). The application of such simplified methodology and the obtained results are described in Section 3.
- the techno-economic optimization of the star receiver design, for a given solar field and location, is performed through a parametric approach and using the LCOH as Key Performance Indicator (KPI) to identify the optimized receiver configuration. The analysis begins with the solar field generation and the optical analysis to assess the heat flux maps on each receiver tube. A reference cylindrical receiver is considered to generate the solar field that is then used for the receiver design optimization. The heat flux maps on each investigated receiver configuration are used as input of the receiver thermal model, that provides as main outputs HTF mass flow rate, thermal efficiency and tube temperature distribution. The methodology continues with the hydrodynamic analysis to assess the HTF pressure distribution and a creep-fatigue analysis aimed at estimating the receiver lifetime. Lastly, an economic analysis is performed to evaluate the LCOH of each investigated receiver design.
- the optimized configuration of star receiver obtained through the approach summarized in the previous point, is then compared from a techno-economic point of view to state-of-the-art external cylindrical receivers.

The methodology proposed to achieve these three objectives is schematically represented in Fig. 2. This study focuses on one particular configuration of star receiver, which is characterized by three rays (or fins) separated by an angle of 120° and has the hydraulic configuration suggested by Binder et al. [15] (see Fig. 3). Three rays are chosen because, when considering a reference cylindrical receiver with identical tube dimensions, they enable a reduction in the number of tubes by half maintaining the same exposed surface and almost the same receiver diameter. The receiver can be oriented either due North or due South, meaning that one of the three rays is directed in the North or South direction. The hydraulic configuration is illustrated in Fig. 3: HTF flow splits in two flow paths before entering from bottom in the two East and West directed rays, thus these are the first two rays in which the fluid simultaneously flows. When the two flow paths exit from each of the first two East-West rays, they mix before entering in the third and last ray. The first two rays have three panels in series while the third one has only two panels due to its larger mass flow rate.

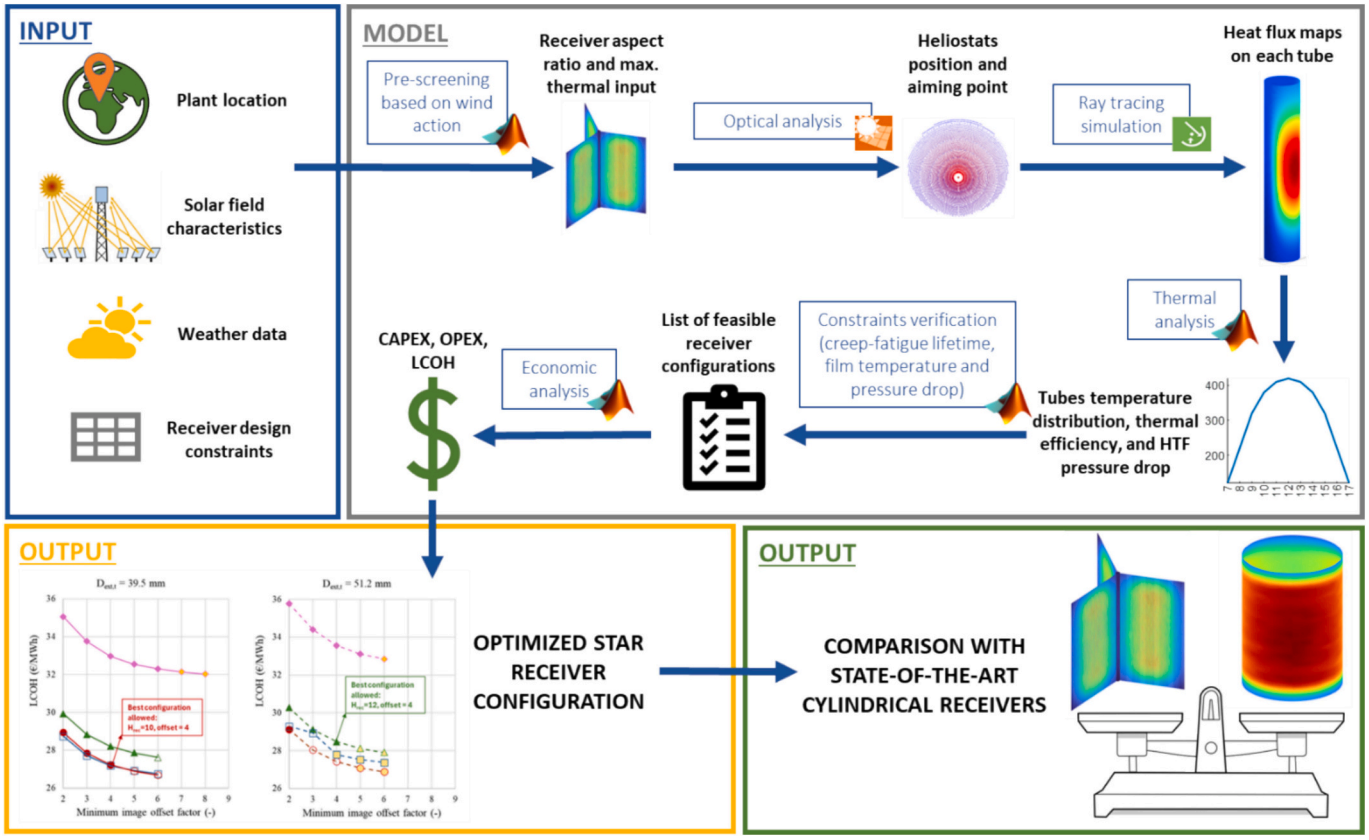

Fig. 2. Scheme of the methodology proposed for the techno-economic optimization of star receivers design.

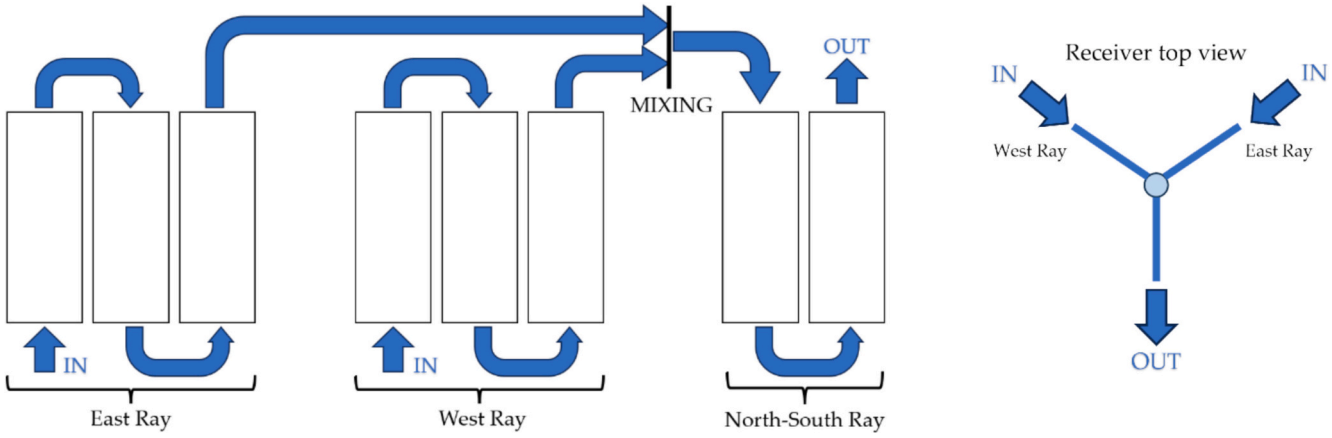

Fig. 3. Example of hydraulic circuitry.

2.1. Wind load

The star receiver is a structure strongly subjected to the wind action since it is placed at a relevant altitude on top of the solar tower (more than 100 m height), where the wind velocity is significantly high, and – differently from conventional cylindrical receivers - the rays must withstand this load without any back support. The proposed method to assess the wind action on the receiver consists of two steps: evaluation of the force generated by the wind is evaluated, and then calculation of the stresses generated inside the structure by the wind force. The method requires as input the receiver characteristics (i.e., tubes material, length, diameter and thickness and distance between adjacent tubes), its operating temperature, and the wind velocity, and it allows to assess whether a given receiver design is able to withstand the wind load or not.

The wind force acting on the receiver is evaluated considering each ray independently and applying the guidelines provided by EUROCODE standard [16] for a structure consisting of many adjacent cylindrical bodies with a certain air gap between them, thus similar to a star receiver ray. To apply such guidelines each ray is treated as if it were alone without the influences of the others. In detail, the wind force is provided by Eq. (1) where ρ is the air density at ambient temperature and pressure, v is the wind velocity at receiver's height,[1] $D_{ext,t}$ is the receiver tubes outer diameter, H_{rec} is the receiver height (i.e., the tubes length), k is a factor accounting for the mutual influences between adjacent tubes equal to 1.15 for the investigated geometry,[2] C_sC_d is the structural factor that accounts for the dynamic response of the structure, and C_f is the force coefficient for vertical cylinders.

$$F = k \cdot C_s C_d \cdot C_f \cdot \left(\frac{1}{2} \cdot \rho \cdot v_{wind}^{\,2}\right) \cdot D_{ext,t} \cdot H_{rec} \tag{1}$$

In detail, C_sC_d considers the effect on wind action of the non-simultaneous occurrence of peak wind pressures on the surface (C_s) together with the effect of the vibrations of the structure due to turbulence (C_d). This parameter is calculated through a set of equations - not reported for sake of brevity - detailed in the EUROCODE standard [16]. This set requires as input receiver geometrical parameters ($D_{ext,t}$, th, H_{rec}), tubes material density, wind velocity (v_{wind}), natural frequency of the structure,[3] and the force coefficient (C_f). The latter represents the drag coefficient of an isolated cylinder that is computed as the product between the force coefficient of an infinitely long cylinder ($C_{f,0}$) and the end-effect factor. $C_{f,0}$ is a function of the Reynolds number and the surface roughness of the tube, it is evaluated through the correlations reported in the EUROCODE standard [16].

As the wind velocity is assumed constant throughout the receiver height, the force per unit length (f) is simply evaluated as the ratio between the overall force (F) and the receiver's height (H_{rec}).

The stresses generated inside the tube walls are evaluated through a simplified one-dimensional analysis based on the beam theory, which allows to determine the maximum axial and tangential stress in each axial section. Those stresses are computed applying the principle of virtual works for a single tube clamped on one side (top) and axially free to move on the other (bottom), as shown in Fig. 4a. As a first approximation, the effect of clips between adjacent tubes or additional support structures along the receiver height on the stresses generated by the wind action is not considered in this work. The resulting beam structure is thus two times hyper-constrained and it can be solved assuming as hyperstatic unknowns a force perpendicular to the structure and a torque. Assuming elastic behavior, without any anelastic distortions and neglecting the tangential stress that is at least two orders of magnitude lower with respect to the axial stress, the axial stress as function of the longitudinal coordinate (z) can be computed through Eq. (2):

$$\sigma_z(z) = \frac{\frac{f}{2} \cdot \left(-z^2 + H_{rec} \cdot z - \frac{H_{rec}^{\,2}}{6}\right)}{\frac{\pi}{32 \cdot D_{ext}} \cdot \left(D_{ext,t}^4 - D_{int,t}^4\right)} \tag{2}$$

The non-dimensional profile of σ_z, with respect to its maximum positive value (in the tubes' middle length), is reported Fig. 4b as function of the non-dimensional axial coordinate (specific to tube length). To verify the structure's mechanical resistance the maximum axial stress in each section σ_z is compared with one third of the ultimate tensile strength σ_{UTS} [17]. This verification applies for both tensile and compressive stresses and, if a symmetric behavior between tension and compression is assumed, it takes the form of Eq. (3).

$$-\frac{\sigma_{UTS}}{3} < \sigma_z < \frac{\sigma_{UTS}}{3} \tag{3}$$

It is important to stress that the approach adopted for calculating axial stress on the tubes due to wind effect assumes that the wind is always perpendicular to the rays of the receiver which is a simplified yet conservative assumption. Under this the drag force is the highest,

[1] The wind velocity at the receiver's height is obtained through the following relation, taken from the EUROCODE standard [16], where $v_{wind,0}$ is the wind velocity at 10 m above the ground: $v_{wind}(z) = v_{wind,0} \cdot 0.19 \cdot ln\left(\frac{z}{0.05}\right)$

[2] According to the EUROCODE standard [16], k is 1.15 when the ratio $(D_{ext,t} + D_{tt})/D_{ext,t}$ is lower than 3.5, where D_{tt} is the distance between adjacent tubes.

[3] The natural frequency is obtained as described by Cammalleri and Costanza, 2016 [47].

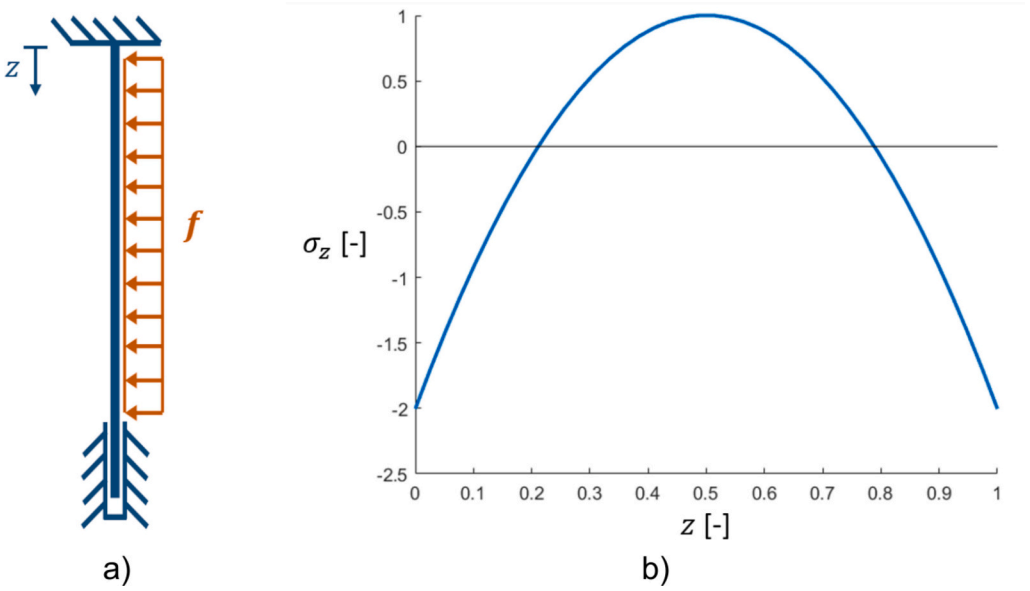

Fig. 4. a) schematic representation of constrained tube under wind load; b) trend of the non-dimensional axial stress generated by the wind load on a receiver tube.

ensuring a prudent estimation of the stresses. If recirculation effects were to be considered, they would reduce the drag force with benefits for the receiver's structural integrity. However, for the sake of simplicity, this effect has not been included in the model. Furthermore, the analysis focuses on the stresses generated directly by the wind on the individual tubes. The moment generated by the wind action on the entire ray is not considered, as it is assumed that the ray is firmly anchored to the central structure of the receiver.

2.2. Optical analysis

The optical analysis consists of two main steps: solar field generation and mirrors' aiming point definition, carried out in SolarPilot [18], and heat flux maps generation determined through raytracing simulation performed in SolTrace [19].

In detail, the solar field is generated according to a reference cylindrical receiver that depends on the investigated case study. This approach can be deemed valid as a first approximation, despite the geometrical differences between the cylindrical and the star-shaped receivers, as long as the aiming points of each heliostat are optimized for the star configuration. Therefore, the star geometry is implemented with the aid of the multi-receiver option of SolarPilot, modelling each ray as two flat side-by-side receivers, attached to a central cylindrical support. The strategy Image Size Priority is used to define the aiming points of each heliostats [20–22].

The solar field with the defined aiming points is then imported in SolTrace [19], where the flat surfaces are replaced with the tubes. A raytracing simulation is then performed to obtain the heat flux maps on each tube. The tubes' coating absorbance is provided as input to SolTrace therefore reflective losses are accurately computed by the software and they are included in the optical efficiency, defined as the ratio between the radiation absorbed by the external surfaces of the receiver tubes and the overall radiation hitting the mirrors. Heat flux maps are then used as input of the receiver thermal model, described in the following section.

2.3. Receiver thermal model

The Star Receiver Thermal Model is a three-dimensional steady-state numerical model implemented in Matlab and it is an extension of the models developed in previous works for external cylindrical receivers [21,23,24] and verified against published results of Computation Fluid Dynamic simulations in [21]. It is designed for a three rays star receiver and allows to investigate any desired configuration in terms of receiver orientation (i.e., one ray toward North or South), HTF entrance (i.e., either from internal or external side of the rays), and number of panels per ray. HTF inlet is assumed to be at the bottom while outlet at the top of the receiver, following a serpentine path through the different panels (see Fig. 3). HTF mass flow rate splits according to the power absorbed by the fluid in the first two rays to have the same mixing temperature before entering the third ray.

The model simulates both flow paths as well as all receiver's tubes, which are discretized in both axial and circumferential directions. Moreover, the external side of the very last tube of each ray is considered adiabatic, due to the presence of pylons installed to support to structure [15].

Each discretized tube element is modeled as a network of thermal resistances, reported in Fig. 5, whose solution provides the different thermal powers used to assess the receiver energy performance and the temperature distributions of tube wall and the HTF. The thermal power absorbed by the HTF is determined by solving the energy balances at node A, representing the tube element's external wall, and node B, representing the mean radius of the tube wall.

Let $p = \{1, 2, \ldots, N_p\}$ and $t = \{1, 2, \ldots, N_t\}$ be the indices indicating the panel and tube, respectively, while $i = \{1, 2, \ldots, N_{ax}\}$, $j = \{1, 2, \ldots, N_c\}$ identify the axial and circumferential position in each tube, the balance at node A includes convective losses ($\dot{Q}_{conv,p,t,i,j}$) radiative losses toward the external environment ($\dot{Q}_{rad_{ext},p,t,i,j}$), and thermal power radiatively exchanged between rays ($\dot{Q}_{rad_{rr},p,t,i,j}$). Convective losses are evaluated considering mixed convection conditions as detailed in previous works [21,22] with the only difference that a fixed heat transfer coefficient is assumed for the forced convection (i.e., 15 $\frac{W}{m^2K}$).

Radiative losses are evaluated, assuming opaque, diffuse, grey, and uniform surfaces, through Eq. (4) where ε_t is the emissivity of the tube surface, T_{surr} is the equivalent surrounding temperature calculated as reported in Gentile et al. [22] and $F_{p,t,i,j\rightarrow ext}$ is the tube element's 2D view factor toward the external environment.

$$\dot{Q}_{rad_{ext},p,t,i,j} = \frac{\sigma \cdot \left(T^4_{ext,p,t,i,j} - T^4_{surr}\right)}{\frac{1-\varepsilon_t}{\varepsilon_t \cdot A_{ext,p,t,i,j}} + \frac{1}{A_{ext,p,t,i,j} \cdot F_{p,t,i,j\rightarrow ext}}} \tag{4}$$

The view factor $F_{p,t,i,j\rightarrow ext}$ is determined using the Hottel's crossed-strings method [25] as schematically represented in Fig. 6. In detail,

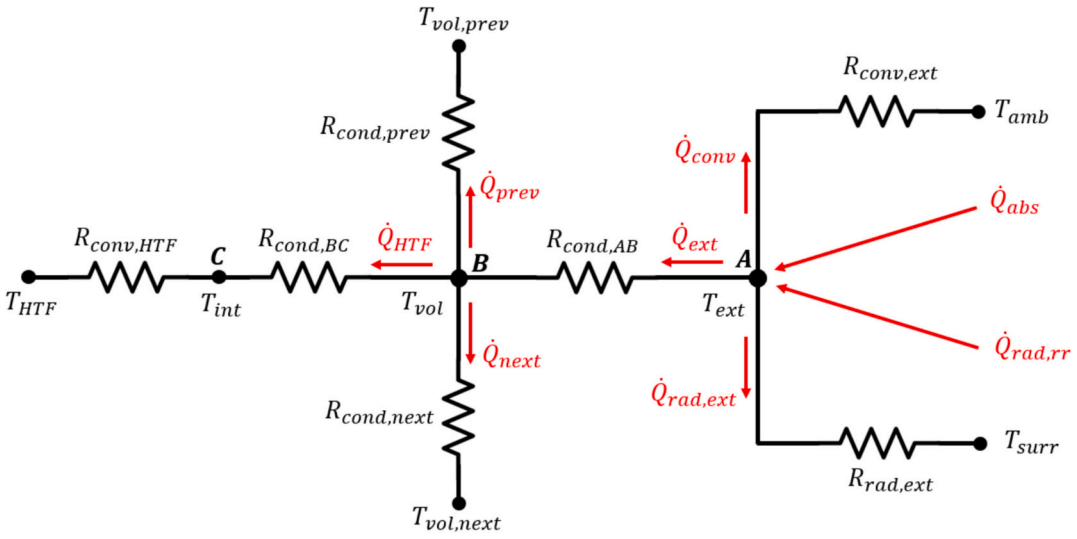

Fig. 5. Network of thermal resistances modelling the p,t,i,j-th tube element.

the latter shows how the view factor between the curve surface AB and the external environment ($F_{AB\to ext}$) is computed, where segment CD represents the maximum portion of the sky visible for any tube. C′ is instead obtained differently depending on the position of A on the tube circumference: it coincides with 1) the intersection between CD and the tangent to the adjacent tube starting in A if the latter does not intersect the tube itself ($\vartheta_A \geq 0^\circ$) or 2) the intersection between CD and the tangent in A to the tube itself, if the previous condition is not satisfied ($\vartheta_A < 0^\circ$). Then, the view factor is obtained applying the typical crossed strings formulation: $F_{AB\to ext} = (BC' + AD - BD - AC')/(2{\cdot}AB)$.

The thermal power lost or absorbed by the tube element due to radiative heat exchange between the next ray ($\dot{Q}_{rad_{rr},p,t,i,j}$) is assessed assuming that each ray is a flat surface at a uniform temperature. In detail, Eq. (5) is employed, where $T_{av,ray}$ and $T_{av,adj,ray}$ are respectively the average temperatures of the side of the ray where the the p,t,i,j-th element is located, and the average temperature of the side of the ray seen by the same element, s_t is the pitch between adjacent tubes, N_{tr} is the number of tubes per ray, and $F_{ray\to ray}$ is the 3D view factor between two facing rays, computed through the Matlab function "*viewfactor*" which enables calculation of three-dimensional view factors between two planar surfaces, regardless of their shape or orientation [26].

$$\dot{Q}_{rad_{rr},p,t,i,j} = \frac{\sigma\left(T^4_{av,adj,ray} - T^4_{av,ray}\right)}{\left(\frac{1-\varepsilon_t}{\varepsilon_t}\frac{}{H_{rec}\ s_t} + \frac{1}{H_{rec}\ s_t\ F_{ray\to ray}} + \frac{1-\varepsilon_t}{\varepsilon_t}\frac{}{H_{rec}\ s_t}\right) N_{ax}\left(\frac{N_c}{2}\right)} \tag{5}$$

As a first approximation, the radiative power exchanged between adjacent tubes in the same panel is neglected as it can be deemed negligible with respect to the power exchanged with the external

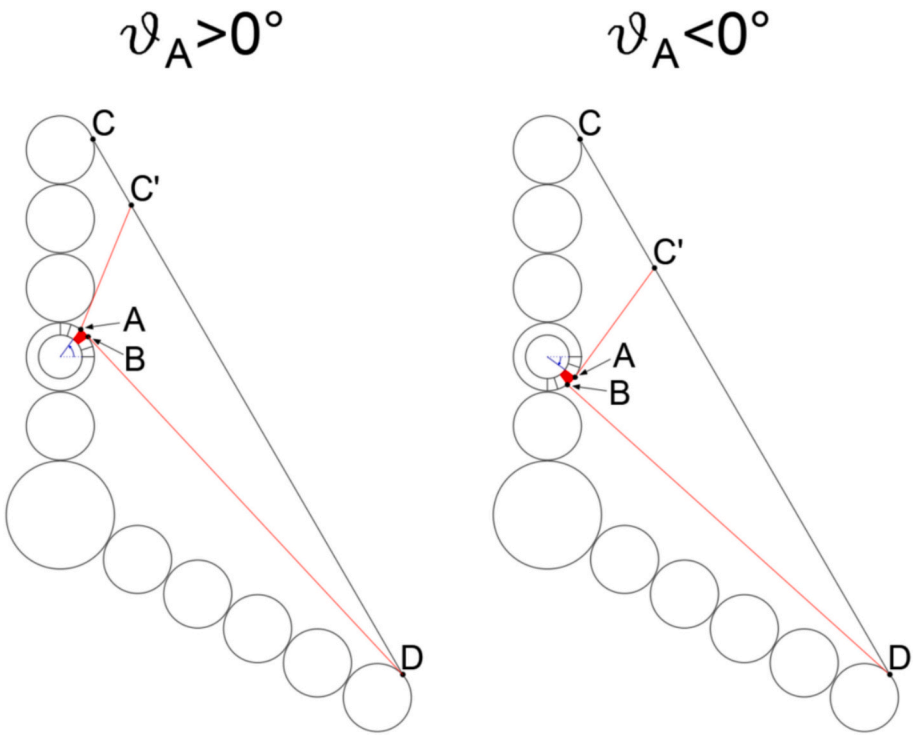

Fig. 6. Crossed string method applied to the generic t,j-th element (figure not in scale).

environment and the other panels.

The power balance at node B is formulated as reported in Gentile et al. [22] accounting for the two-dimensional heat conduction within the tubes as well as for internal heat transfer resistance of the fluid.

The thermal model requires as input receiver geometry, tubes material characteristics, HTF inlet and outlet nominal temperature, ambient conditions and heat flux maps on the receiver. The model is implemented in MATLAB and is based on the following solving procedure. The HTF mass flow rate in each flow path are initialized to first guess values, while the thermal power terms exchanged between neighbor rays are initialized to zero. Then, for each element, the tubes external wall temperature is initially assumed to evaluate the convective and radiative heat exchange and solve the power balances equations as detailed in the previous section. The resulting HTF bulk temperature is used to compute a new value of external wall temperature until the new values differ from the old ones by less than a defined tolerance.

When every panel is solved and receiver outlet is reached, the HTF outlet temperature as well as the thermal power exchanged between neighbor rays are evaluated and a new iteration is performed with updated mass flow rate until convergence is achieved on all of them.

The main output of the model are the receiver thermal efficiency (i.e., thermal power absorbed by HTF divided by thermal power absorbed by the tubes outer walls), tubes and HTF temperature distribution as well as HTF mass flow rate.

2.4. Hydrodynamic analysis

The hydrodynamic analysis estimates HTF pressure drop in the receiver and evaluates the pumping electric power required for its circulation. The overall HTF pressure drop in both tower and receiver under design conditions (Δp_{HTF}^{des}) is evaluated considering three contributions: i) pressure drop in the tower due to the geodetic head; ii) distributed pressure drop in tubes, headers and manifolds that is evaluated assuming that headers and manifolds are sized to have the same HTF velocity of the tubes; and iii) concentrated pressure drop in the receiver that is computed accounting for the curves and connections detailed in the previous study on external cylindrical receiver [22] plus the mixing occurring at the inlet of the third ray. The mixing pressure drop is evaluated based on the pressure loss coefficient formulation provided by Levin [27].

Finally, the HTF pumping electric consumption, for each operating condition, is computed by means of Eq. (6) where $\dot{m}_{HTF}$ is the HTF mass flow rate flowing in the receiver in each time step, $\dot{m}_{HTF}^{des}$ and Δp_{HTF}^{des} are the HTF mass flow rate and pressure drop in design conditions, $\rho_{HTF,T_{min}}$ is the HTF density at the receiver inlet temperature, and η_{pump} is the pump efficiency accounting for hydraulic and electro-mechanical losses:

$$P_{el,pump} = \frac{\dot{m}_{HTF}^{3} \cdot \Delta p_{HTF}^{des}}{\rho_{HTF,T_{min}} \cdot \eta_{pump} \cdot \dot{m}_{HTF}^{des\ 2}} \tag{6}$$

In detail, both the design ($\dot{m}_{HTF}^{des}$) and hourly ($\dot{m}_{HTF}$) mass flow rates of HTF are evaluated through the thermal and optical analyses described in the previous sections, while the pump efficiency and the HTF density will depend on the analyzed case study (see Section 4).

2.5. Creep-fatigue lifetime

Once optical, thermal and hydrodynamic performances are evaluated, receiver's creep-fatigue lifetime is assessed through the mechanical model developed and extensively described in previous works [21,22,28].

In this study, the creep and fatigue damage accumulation is only analyzed for a clear-sky representative day and is then extended to the entire year by assuming that, in one year, the receiver operates for $N_{d,y}$ identical days where $N_{d,y}$ is obtained as the ratio between the overall yearly irradiation and the average daily one. A more accurate lifetime estimate may be obtained at the expense of computational time by simulating the receiver for multiple days or an entire typical year.[4] For each hour of the representative day, thermal stresses distribution in the tubes is evaluated through the methodology proposed by Logie et al. [29] and are summed to the membrane stresses due to HTF pressure computed through the thick wall formulation adopted by Neises et al. [30].

The Logie et al. [29] method is based on the plane-biharmonic thermoelastic approach and assumes that the tube cannot displace perpendicularly to the axial direction (infinite clip along its length). In external cylindrical receivers, tubes are not continuously guided along their length, however, to prevent excessive panel bowing or tubes overheating by contact, their movement is restricted by a series of welded supports, called clips, which induce additional mechanical stresses [7]. In star-shaped receivers, tubes exhibit much lower circumferential thermal gradients compared to conventional cylindrical receivers. This results in a significantly reduced tendency for tube deformation, thereby minimizing the need for clips or other structural support mechanisms. Nonetheless, this study does not focus on these detailed engineering design aspects, as it is instead focused on showing the benefits of this innovative configuration, which will still need in-depth pre-construction structural investigations. Therefore, the effect of clips or additional support structures on tubes thermal stresses is not considered in this work. However, in a previous work thermal stresses obtained through the Logie et al. [29] method for cylindrical receiver tubes were compared to finite element analyses' results obtained considering the effect of clips, and the maximum error on the equivalent Von Mises stress was about 13 % [21]. For star receivers, since the circumferential thermal gradients are lower than in cylindrical receivers, the tubes are closer to the "infinite clip along their length" condition. As a result, it is expected that the error in the Von Mises stress calculation for the star receiver will not lower, therefore not exceeding the 13 % observed for cylindrical receivers. As far as the fatigue damage is concerned, one fatigue cycle per day is considered, from a zero-stress condition to the maximum elastic axial stress experienced during the day. The elastoplastic strain range associated with that fatigue cycle is evaluated using the Neuber's rule [7] coupled with the Bree diagram [31] to distinguish the elastoplastic regime.[5]

The creep damage is instead evaluated through the same procedure described in previous works that accounts for the redistribution of stresses due to plastic deformation as well as for the stress relaxation induced by creep [21,22,28].

Then, the creep-fatigue lifetime is obtained using the widely adopted creep-fatigue interaction diagram [32]: the number of years after which failure occurs in each receiver location is defined as the number of years (N_y) after which the accumulated creep and fatigue damages ($N_{d,y}$ times the daily damages) individuate a point outside the damage envelope.

2.6. Economic and yearly analyses

The goal of the economic analysis is to assess the LCOH of the generated thermal energy, that is defined by Eq. (7) where CAPEX and OPEX only refer to the components needed to convert the sun power into heat. The LCOH is chosen as KPI for the receiver design optimization instead of the commonly adopted Levelized Cost Of Electricity (LCOE),

[4] A similar approximation was used in a previous work [21], where the receiver operation was simulated considering 365 clear-sky days per year obtaining errors on the estimated lifetime of about 30 % with respect to a three-days clustering approach.

[5] The elastoplastic regime is evaluated based on the maximum thermoelastic axial stress ($\sigma_z^{T,E}$): if $\sigma_z^{T,E} < 2S_y$ (elastic or elastic shakedown regimes) the strain range is computed according to the Hooke's law, otherwise (plastic cycling) it is obtained through the Neuber's method for cyclic loading [7].

which would require the design and cost assessment of the other plant components which are invariant to the receiver design. Therefore, the results of the receiver design optimization would not change adopting LCOH instead of LCOE with the benefit of reducing the calculation efforts and number of assumptions made.

The CAPEX is evaluated starting from the Total Equipment Cost (TEC) through Eq. (8) where c_{cont} and c_{EP} are the contingency and engineering and procurement costs [33].

TEC is estimated summing the costs of receiver (C_{rec}), solar field (C_{SF}), tower (C_{tow}), horizontal piping (C_{pip}), cold salt pumps (C_{pump}), control system (C_{contr}), and spare parts (C_{spare}) [4]. The receiver cost (C_{rec}) is assessed through Eq. (9), where $C_{rec,eng}$ is a fixed engineering cost,[6] c_{met} is the metal cost of the selected material that multiplies the total mass M_{met} of tubes, headers and manifolds,[7] CF is a correction factor that relates the material cost of tubes, headers and manifolds to the receiver cost,[8] $c_{coat,purch}$ and $c_{coat,app}$ are the receiver coating (Pyromark 2500) purchasing and application costs taken from Ho and Pacheco [34] and equal to 4.95 €/m^2 and 262.6 €/m^2 respectively, and A_{coat} is the coated area (i.e., number of tubes times tubes lateral area). All specific costs are adjusted to 2020 using the Chemical Engineering Plant Cost Index (CEPCI) [35].

All the other costs contributing to the TEC, as well as OPEX and Capital Recovery Factor (CRF, which is the CAPEX actualization accounting for discount and inflation rates) are assessed as described in the previous work [22].

$$LCOH = \frac{CRF \cdot CAPEX + OPEX}{Q^{y}_{HTF}} \tag{7}$$

$$CAPEX = TEC \cdot (1 + c_{cont}) \cdot (1 + c_{EP}) \tag{8}$$

$$C_{rec} = C_{rec,eng} + c_{met} \cdot m_{met} \cdot CF + A_{coat} \cdot \left(c_{coat,purch} + c_{coat,app}\right) \tag{9}$$

Q^{y}_{HTF} is the yearly available thermal energy that is evaluated by means of a simplified yearly analysis performed on hourly basis for a reference day. Given the DNI profile for a reference clear sky day at spring equinox, $\dot{Q}^{y}_{HTF}$ is estimated according to Eq. (10) [22] that takes into account the impact of the HTF pumping electric consumption on the LCOH. In detail, $\dot{Q}_{HTF}$ and $P_{el,pump}$ are the thermal power absorbed by the HTF and the electric power consumed by pumps in each hour of the investigated day, respectively, Δt is the time step size (i.e., one hour), day_{eq} represents the number of equivalent days in one year defined as the ratio between yearly and daily irradiation, h is the index indicating the hour of the day (from 7 am to 5 pm), and η_{PB} is the power block efficiency determined as the product between the power block second law efficiency and the Lorentz's cycle efficiency. The latter is assed computing the mean logarithmic temperature as function of HTF inlet and outlet receiver temperature [22].

$$Q^{y}_{HTF} = \left(\sum_{h=7}^{17} \left(\dot{Q}_{HTF} - \frac{P_{el,pump}}{\eta_{PB}} \right) \cdot \Delta t \right) \cdot day_{eq} \tag{10}$$

[6] Taken from the 2010 contract report by Abengoa Solar which documented the estimated cost for solar tower plants with conventional and supercritical coolants, and equal to 3.89 M€ [8].

[7] Headers and manifolds internal diameters are selected in order to have a HTF velocity as close as possible to that inside the tubes [8] and their thickness is selected from the Rolled Alloys pipe size chart [40]. Headers are assumed to have the same length of panels while manifolds are longer due to their two 90° curves, where the curvature radius is assumed equal to the manifold diameter.

[8] it is determined based on the Abengoa report [8] and it is equal to the ratio between the reported cost of a conventional cylindrical nitrate salt receiver (excluding engineering and coating) and its material cost, resulting 21.9. This approach can be considered valid, as a first approximation, since panels manufacturing cost is the same of cylindrical receivers one despite their arrangement is different in star receivers [15].

3. Maximum receiver size

In this section the procedure described in the Section 2.1 is applied to find the maximum allowable receiver size - in terms of receiver incident thermal power $\dot{Q}_{rec}$ - that can withstand the wind action. The variables affecting the resulting tube stresses are: tower height, ground-level wind velocity (v_0), and tubes material, diameter ($D_{ext,t}$), thickness (th), and length (equal to receiver's height H_{rec}) with the latter being the most crucial parameter as it affects the stress with a quadratic dependency.

The analysis is performed fixing the average heat flux incident on the receiver and varying the receiver aspect ratio (AR = 1, 1.5, 2), the tubes outer diameter ($D_{ext,t}$ = 10.3 mm, 39.5 mm, and 51.2 mm[9]), the average heat flux on the receiver, and the tubes material. As far as the latter is concerned, three candidate materials are investigated: Inconel 740H, Haynes 230, and Incoloy 800H. 740H is extensively used in steam boilers [36] and it resulted the best candidate material for external receivers among five different alloys compared by Laporte-Azcué et al. [36] Haynes 230 (H230), traditionally used in gas turbines, is recently considered for CSP applications thanks to its good corrosion resistance and thermal stability [7,37]. 800H is recommended for corrosive and high temperatures environments and was used to manufacture the steam receiver of the Solar One project [36].

The plant is assumed to operate in Sevilla where the maximum velocity at 10 m above the ground is 13.4 m/s [20]; the tower height is conservatively assumed equal to 200 m where the wind velocity is 21.1 m/s.[10]

For each investigated configuration, the receiver thermal input is increased - with a 5-MW$_{th}$ increment - from 5 MW$_{th}$ to 1000 MW$_{th}$, the receiver height and diameter are determined based on the assumed AR and average heat flux, and the maximum thermal input that can withstand the wind load is stored in a matrix. To verify whether a design withstands the wind load or not the maximum axial stress is compared with one third of the UTS. The latter is evaluated both at 700 °C and 30 °C in order to consider the scenario in which during highly windy days the receiver is shut down to enhance its wind resistance.

The results obtained for an average heat flux on the receiver of 600 kW/m^2 are shown in Fig. 7 which points out that each of investigated design choices plays an important role in defining the wind load resistance:

1. low aspect ratio are beneficial: AR = 1 entailing about twice the resistance of AR = 2;
2. large tubes are preferrable: 51.2 mm tubes provide from 8 to 15 times higher maximum thermal input than 10.3 mm ones; these results are in line with what observed by Binder et al. [15],
3. better performing materials leads to larger allowable receivers: at 700 °C, 800H shows a maximum thermal input of 445 MW$_{th}$, followed by H230 with 820 MW$_{th}$, and 740H exceeding 1000 MW$_{th}$.

It is important to notice that a 50 % lower average hear flux would mean a 50 % lower maximum thermal power.

4. Case study

The methodology described in the previous sections is applied to a specific case study to optimize the design of a solar salt star-shaped

[9] 10.3 mm represents a small size that is evaluated to demonstrate the significant impact of this design parameter on the wind load resistance, while 39.5 mm and 51.2 mm are the dimensions adopted in the Gemasolar and Crescent Dunes commercial plants, respectively [21,39]. The tubes thicknesses associated with each diameter are 0.89, 1.65 and 1.65 mm, respectively.

[10] The impact of the tower height is limited, as a 100 m tall tower would have a wind velocity of 19.4 m/s.

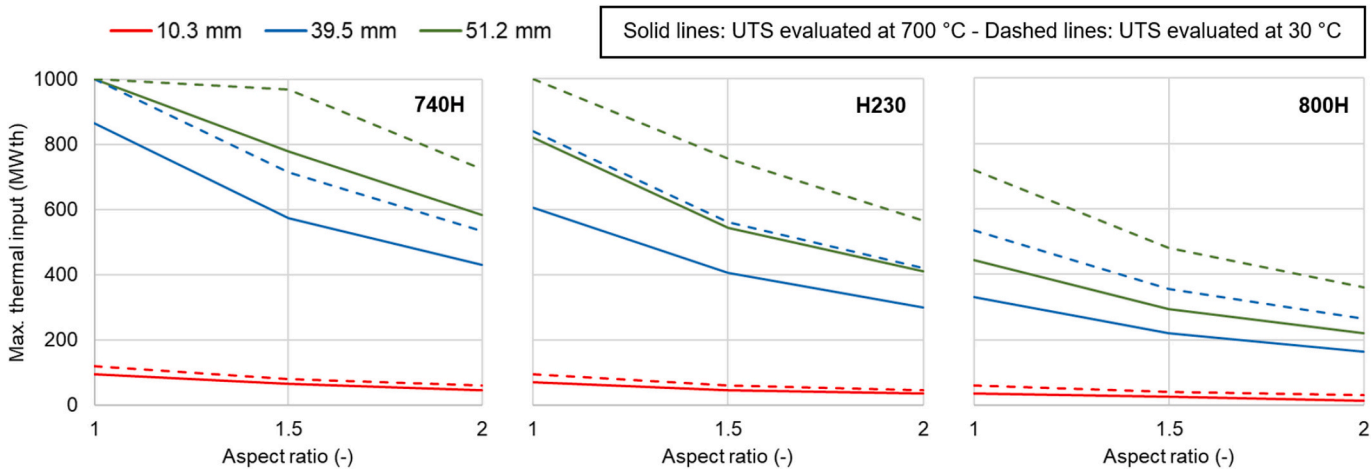

Fig. 7. Maximum thermal input allowed for each combination of aspect ratio, tubes outer diameter, and tubes material. Average heat flux is 600 kW/m^2; the maximum investigated thermal input is 1000 MW$_{th}$.

receiver for a given solar field and plant location. The optimization is based on the parametric analysis and is performed varying the receiver's height (H_{rec}) and tubes diameter ($D_{ext,t}$) and evaluating the LCOH of each of combination. For each investigated design the minimum image offset factor for the heliostats aiming strategy is also optimized based on the LCOH. This parameter is required by SolarPILOT when the strategy "*Image Size Priority*" is adopted and is used to define the minimum distance between the image centroid and the edge of the receiver aperture to reduce spillage; a higher offset results in a more concentrated heat flux in the receiver central part, with higher peak values and lower spillage losses [20]. The receiver aspect ratio is fixed to one according to the results of Section 3. Receiver orientation and hydraulic configuration (i.e., number of panels per ray) is taken from Binder et al. [15], according to which the best configuration is oriented due South (in the North hemisphere) and it has five panels in the first two East-West rays and two panels in the third ray, with the HTF entering from the external side of the rays. The number of tubes per ray is univocally determined starting from receiver diameter and tubes outer diameter.[11]

Moreover, the configurations which do not fulfill one of the following conditions are excluded from the analysis: i) the receiver must be able to withstand the wind load, ii) the lifetime must be higher than the plant target life (i.e., 30 years), iii) the maximum design film temperature ($T^{des}_{film,max}$) must be lower than the allowable limit ($T^{des}_{film,lim}$), and iv) the receiver design pressure drop (Δp^{des}_{rec}) must be lower than the allowable limit.

Based on the results of Section 3, a receiver size up to 1000 MWth can be investigated. Since in the optimization phase the receiver configuration is varied, it is safer to consider a size that is far from the maximum one, in order to have more degrees of freedom without overcoming the constraint of the wind load resistance. Thus, a plant similar to the Gemasolar Thermosolar Plant, operating in Sevilla since May 2011 and with a receiver size of 184 MW [38], is considered as case study. The main characteristics of this plant are taken from Binotti et al. [38,39] and reported in Table 1.

As anticipated, the solar field is fixed during the optimization procedure. However, considering a reproduction as faithful as possible of the Gemasolar's solar field (see Fig. 8a) would entail not to take full advantage one of the most important features of star receivers. In fact, as discussed extensively in this article, the main strength of star receivers is to allow a uniform flux distribution around the tube surface, and such uniformity is best achieved with a perfectly surrounded field. To better investigate this aspect, a preliminary analysis is performed, comparing a Gemasolar-like solar field with another solar field, hereby referred to as surrounded solar field, having the same number and type of mirrors and tower height, but generated so as to be perfectly circular with a field radius equal to the Gemasolar's southern one (i.e., 600 m) (see Fig. 8b). For the solar fields generation, the receiver characteristics in Table 1 are considered, the plant is assumed to be located in Sevilla, and spring equinox with a design DNI of 950 W/m^2 is take as design condition.

Table 1
Main characteristics of the Gemasolar plant [38,39].

Item	Symbol	Value	UoM
Location	–	Seville	–
Tower optical height	$H_{tow,opt}$	124	m
N° of mirrors	N_{mirr}	2650	–
Heliostat width	W_{helio}	11	m
Heliostat height	H_{helio}	10	m
Mirror reflectivity	ρ_{helio}	0.93	–
Mirror optical error	–	3.4	mrad
Receiver diameter	D_{rec}	8	m
Receiver height	H_{rec}	16	m

Results of this preliminary analysis show that the surrounded field leads to a 1.7 % higher optical efficiency and a comparable thermal efficiency, resulting in a 1.88 % lower LCOH. Therefore, the surrounded solar field is considered for the received design optimization.

Based on the considerations reported in the previous section, three materials are analyzed: Inconel740H, Haynes230, and Incoloy800H. For each of the three materials 12 different receiver configurations are investigated (four receiver heights times three tubes outer diameters), and for each of them the optimized image offset factor is individuated varying it between 2 and 9 with an increment of one.

The investigated tube diameters are taken from standard commercial sizes [38,40,41] and are 26.7 mm, 39.5 mm, and 51.2 mm; smaller diameters are not investigated based on the results obtained in Section 3. The thickness of each tube is assumed constant and is 1.65 mm. The distance between two adjacent tubes is considered a fixed design parameter, assumed equal to 2 mm [22,42]. The receiver height is varied among 8 m, 10 m, 12 m, and 16 m.

Only three and four values of tubes outer diameters and receiver height are investigated as the main goal of the analysis is demonstrating

[11] As the aspect ratio is initially fixed to one and there are five panels in the East-West rays and two panels in the South ray, the number of tubes per ray is obtained as the multiple of ten that leads to a receiver external diameter ($2r_{ray} + 2r_{supp}$) as close as possible to $H_{rec}/2$. The radius of the central support (r_{supp}) is assumed to be five times the tubes outer diameter. Once the number of tubes per ray is determined the actual receiver diameter and aspect ratio can be computed. As a result, the actual aspect ratio will be slightly different from 1.

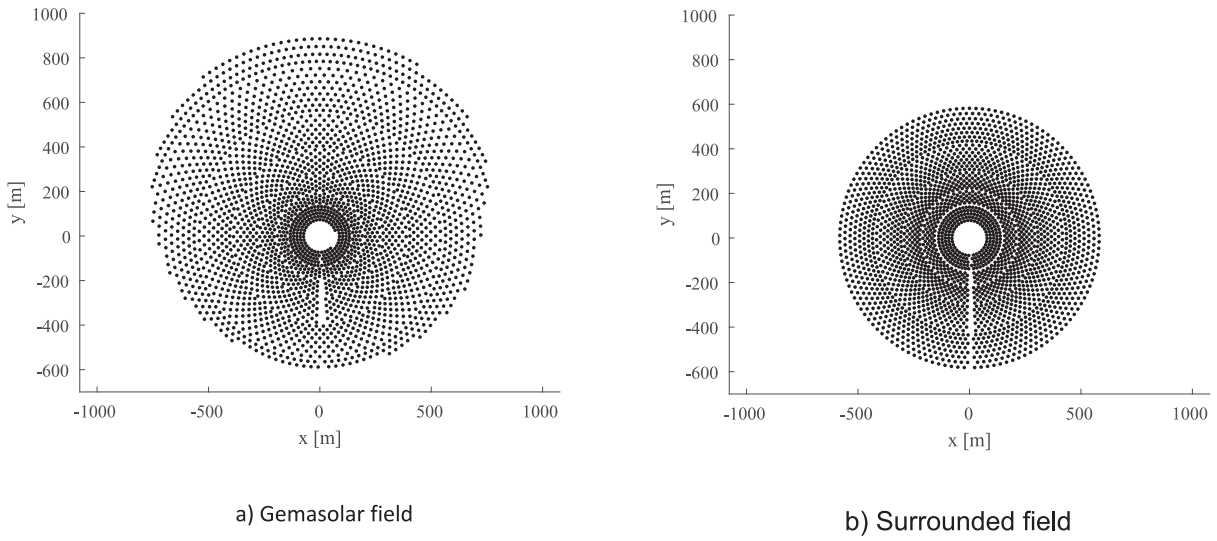

Fig. 8. Solar fields investigated in the preliminary analysis.

the potential of the developed methods, rather than testing every possible combination of receiver to optimize its design in detail. Such a coarse discretization of these two design parameters allows, on the other hand, to keep reasonable computational time.

For all the investigated materials the maximum allowable film temperature ($T^{des}_{film,lim}$) is 650 °C [37]. All material optical and thermo-mechanical properties as well as coefficients for the creep-fatigue lifetime assessment and HTF (i.e. solar salts) thermodynamic properties are taken from a previous work [22]. Based on the same work the alloys costs are assumed equal to 82.6 €/kg, 76.5 €/kg, and 20 €/kg for 740H, H230, and 800H, respectively, the maximum receiver pressure drop is set to 30 bar, the ambient temperature is assumed constant and equal to 25 °C, and tubes coating (Pyromark 2500) absorptivity (α_c) is assumed equal to 0.93.

Internal support is also coated with a white Pyromark 2500 Series coating with a reflectivity of 0.8 [6]. Tubes are discretized in 40 axial (N_{ax}) and 20 circumferential (N_c) elements. Weather data in Sevilla are taken from Energy Plus [43] and the reference clear sky day is assumed to be the 21st of March, whose DNI trend is symmetric with respect to solar noon and has the following trend from 7 a.m. to 12 p.m. (solar time): 542 W/m^2, 690 W/m^2, 788 W/m^2, 858 W/m^2, 902 W/m^2, 917 W/m^2. The second-law efficiency of the power block has been assumed equal to 67.6 % to match the average power cycle efficiency obtained at different temperature levels by Manzolini et al. 2019 [44]. The pump hydraulic and electro-mechanic efficiency is assumed equal to 77 %.

The optimized star receiver is eventually compared from a techno-economic point of view to state-of-the-art cylindrical external receivers of the Gemasolar power plant whose characteristics are taken from Binotti et al. [38,39]. The cylindrical case is analyzed using SolarPILOT for the optical efficiency assessment and thermal and mechanical models developed in a previous work [22] to assess thermal efficiency, pressure drop, creep-fatigue lifetime, and costs.

5. Results and discussion

5.1. Receiver design optimization

For each material and for each of the 12 configurations investigated, the minimum image offset factor used for the heliostats aiming strategy[12] were firstly varied from 2 to 6, and then the simulations were extended to higher offset values only for some of the designs. Indeed, for some configurations already with an offset of lower than or equal to 6 the receiver did not fulfill one of the design constraints, namely due to too high film temperature, too high pressure drop or too low creep-fatigue lifetime; as the offset increases the constraints can only be even less respected,[13] therefore investigating higher offsets would not have led to feasible configurations. This is explained in Fig. 9 focusing on the cases with H230 as tubes material but analogous considerations can be made for the other materials.

For instance, the configuration with H230, receiver height of 10 m and tubes outer diameter and 39.5 mm, was only simulated with offset values up to 6, since values above 4 would have led already to lifetimes below 30 years even though with lower LCOH.[14] Differently, the configuration with H230, receiver height of 16 m, and 26.7 mm tubes, does not achieve any of the constraints with offset between 2 and 6, therefore simulations were run with offset up to 9: results showed that with offset equal to 9 the receiver experiences too high film temperatures at design conditions, therefore 8 was chosen as final value for this configuration. In general, the results show that higher offset leads to lower LCOH due to the increase in optical efficiency.

The results of the techno-economic optimization can be summarized in three lists, one per material, of the 12 receiver designs ranked on the basis of the LCOH and with each design associated the optimized image offset factor. Such lists are provided in Table 2, Table 3, and Table 4 that show how, for all configurations, the optimization is remarkably affected by constraints on pressure drop, film temperature and lifetime, highlighting how important it is to address such thermo-mechanical aspects to design star receivers. The lowest LCOH is obtained with 800H as tubes material pointing out the potential of this novel receiver concept to reduce the technology costs using less expensive materials than those typically considered for CSP applications [36,45]. Its value is

[12] As described in Section 4, this parameter is adopted to define the minimum distance between the image centroid and the edge of the receiver aperture.

[13] Higher offset means higher peak heat flux that leads to i) larger thermal stress and, as a consequence, lower creep-fatigue lifetime and ii) higher film temperatures; on the other hand, higher offset means higher optical efficiency that comes with a higher receiver thermal input; the latter leads to a higher HTF mass flow rate and thus higher HTF velocity, resulting in higher pressure drop.

[14] As described in the Section 2, the LCOH does not take into account the maintenance costs associated with tubes or panels replacements when creep-fatigue lifetime failure occurs.

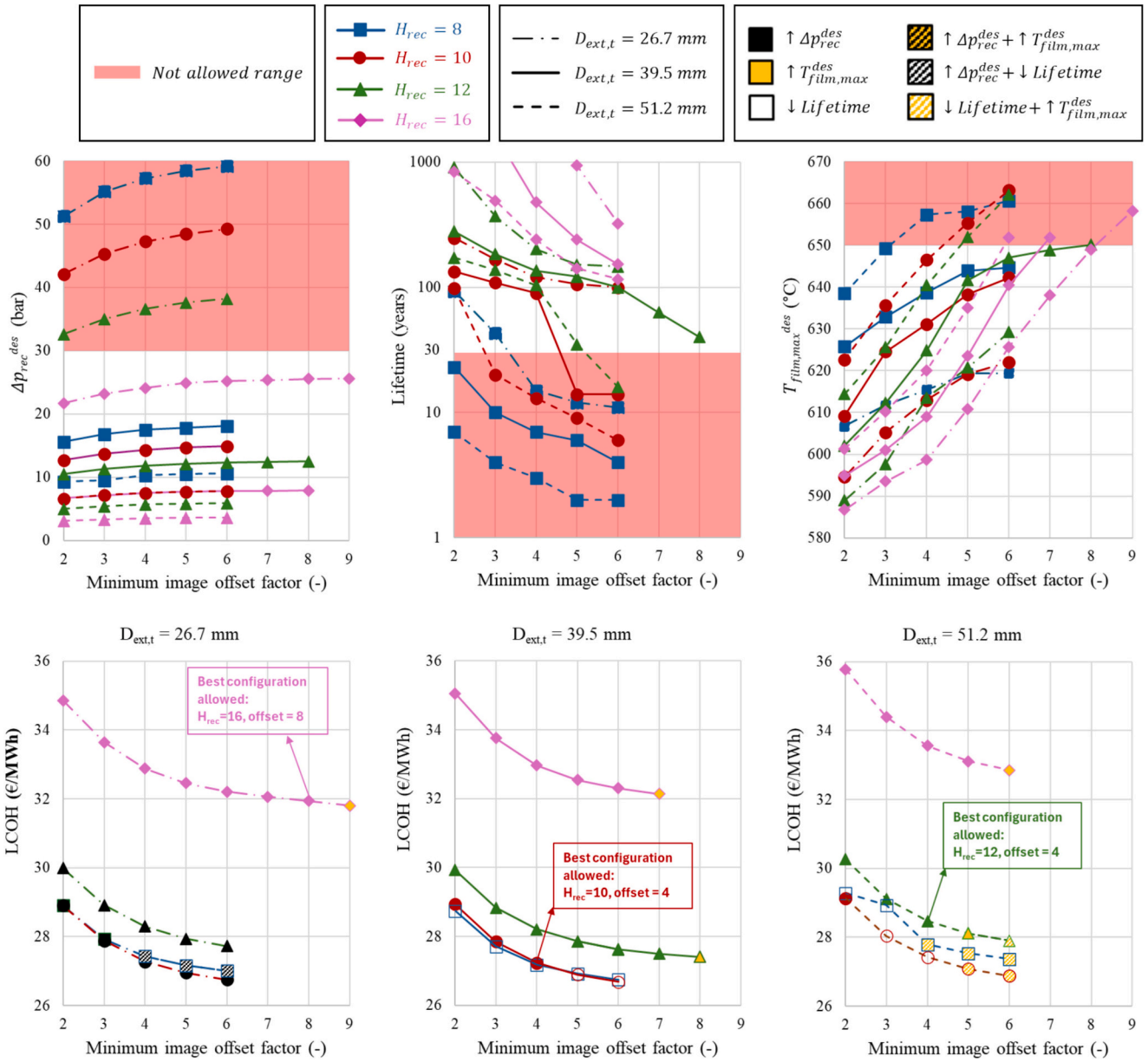

Fig. 9. Summary of the design optimization results with Haynes 230. Top: design pressure drop within the receiver, lifetime and maximum film temperature as function of the minimum image offset factor; Bottom: LCOH as function of the minimum image offset factor for different tubes outer diameters. The symbols $\uparrow \Delta p_{rec}^{des}$, $\uparrow T_{film,max}^{des}$, ↓Lifetime indicate that the configuration has been excluded due to too high receiver design pressure drop, too high receiver design film temperature, or too low creep-fatigue lifetime, respectively, or because of two of these causes together.

Table 2
Optimization results ranked on the basis of the LCOH (740H). The symbols in the column "Notes" refer to the reason why the cases with offset equal to the value in the table plus one were excluded.

#	H_{rec}	$D_{ext,t}$	N_{tr}	Offset	q''_{max}	η_{opt}^{des}	η_{th}^{des}	η_{stt}^{des}	Δp_{rec}^{des}	$T_{film,max}^{des}$	Lifetime	C_{rec}	LCOH	Notes
[−]	[m]	[mm]	[−]	[−]	$[\frac{kW}{m2}]$	[%]	[%]	[%]	[bar]	[°C]	[years]	[M€]	$[\frac{€}{MWh}]$	
1°	10	39.5	120	11	1528	56.6	94.7	53.6	15.2	643.5	58	16.2	26.1	
2°	8	39.5	100	5	1755	51.9	95.7	49.7	17.8	644	30	12.3	26.8	↓*Lifetime*
3°	10	51.2	90	4	1179	54.3	94.4	51.2	7.5	646.5	93	16.2	27.3	$\uparrow T_{film,max}^{des}$
4°	12	39.5	140	7	1072	58.1	93.3	54.2	12.4	649	178	20.8	27.3	$\uparrow T_{film,max}^{des}$
5°	12	51.2	110	4	857	57	92.8	52.9	5.7	640.5	256	21.6	28.3	$\uparrow T_{film,max}^{des}$
6°	8	51.2	70	2	1396	47.4	95.5	45.3	9.3	638.5	74	11.7	29.2	↓*Lifetime*
7°	16	26.7	280	8	819	60.2	89.7	54.0	25.5	649.1	935	32.4	31.6	$\uparrow T_{film,max}^{des}$
8°	16	39.5	190	6	670	60.5	89.4	54	7.8	640.5	521	33.8	32.0	$\uparrow T_{film,max}^{des}$
9°	16	51.2	150	5	577	60.4	88.8	53.6	3.6	635.1	539	35.5	32.8	$\uparrow T_{film,max}^{des}$
–	8	26.7	140	$\uparrow \Delta p_{rec}^{des}$ regardless the offset									–	
–	10	26.7	170	$\uparrow \Delta p_{rec}^{des}$ regardless the offset									–	
–	12	26.7	210	$\uparrow \Delta p_{rec}^{des}$ regardless the offset									–	

Table 3
Optimization results ranked on the basis of the LCOH (H230). The symbols in the column "Notes" refer to the reason why the cases with offset equal to the value in the table plus one were excluded.

#	H_{rec}	$D_{ext,t}$	N_{tr}	Offset	q''_{max}	η_{opt}^{des}	η_{th}^{des}	η_{stt}^{des}	Δp_{rec}^{des}	$T_{film,max}^{des}$	Lifetime	C_{rec}	LCOH	Notes
[−]	[m]	[mm]	[−]	[−]	$[\frac{kW}{m2}]$	[%]	[%]	[%]	[bar]	[°C]	[years]	[M€]	$[\frac{€}{MWh}]$	
1°	10	39.5	120	4	1159	54.6	94.5	51.6	14.3	631.2	90	16.6	27.2	↓*Lifetime*
2°	12	39.5	140	7	1072	58.1	93.3	54.2	12.4	649.0	63	21.3	27.5	$\uparrow T_{film,max}^{des}$
3°	12	51.2	110	4	857	57	92.8	52.9	5.7	640.5	104	22.2	28.5	$\uparrow T_{film,max}^{des}$
4°	10	51.2	90	2	944	51.2	94.1	48.2	6.6	622.7	98	16.6	29.1	↓*Lifetime*
5°	16	26.7	280	8	819	60.2	89.7	54.0	25.5	649.1	170	33.3	31.9	$\uparrow T_{film,max}^{des}$
6°	16	39.5	190	6	670	60.5	89.4	54	7.8	640.5	153	34.8	32.3	$\uparrow T_{film,max}^{des}$
7°	16	51.2	150	5	577	60.4	88.8	53.6	3.6	635.1	142	36.5	33.1	$\uparrow T_{film,max}^{des}$
–	8	26.7	140	$\uparrow \Delta p_{rec}^{des}$ regardless the offset + ↓*Lifetime* with offset above 3									–	
–	8	39.5	100	↓*Lifetime* regardless the offset									–	
–	8	51.2	70	↓*Lifetime* regardless the offset + $\uparrow T_{film,max}^{des}$ with offset above 3									–	
–	10	26.7	170	$\uparrow \Delta p_{rec}^{des}$ regardless the offset									–	
–	12	26.7	210	$\uparrow \Delta p_{rec}^{des}$ regardless the offset									–	

Table 4
Optimization results ranked on the basis of the LCOH (800H). The symbols in the column "Notes" refer to the reason why the cases with offset equal to the value in the table plus one were excluded.

#	H_{rec}	$D_{ext,t}$	N_{tr}	Offset	q''_{max}	η_{opt}^{des}	η_{th}^{des}	η_{stt}^{des}	Δp_{rec}^{des}	$T_{film,max}^{des}$	Lifetime	C_{rec}	LCOH	Notes
[−]	[m]	[mm]	[−]	[−]	$[\frac{kW}{m2}]$	[%]	[%]	[%]	[bar]	[°C]	[years]	[M€]	$[\frac{€}{MWh}]$	
1°	12	39.5	140	7	1072	58.2	93.9	54.6	12.4	648.9	31	8.1	23.2	↓*Lifetime*
2°	10	39.5	120	3	1105	53.4	94.5	50.4	13.7	624.5	44	6.9	24.5	↓*Lifetime*
3°	12	51.2	110	4	857	57	92.8	52.9	5.7	640.5	40	8.2	23.9	↓*Lifetime*
4°	16	39.5	190	6	670	60.5	89.4	54.1	7.8	640.4	91	11.1	24.6	$\uparrow T_{film,max}^{des}$
5°	16	26.7	280	8	819	60.2	89.7	54.0	25.6	649.0	97	10.8	24.6	$\uparrow T_{film,max}^{des}$
6°	16	51.2	150	5	577	60.4	88.9	53.7	3.6	635.1	101	11.5	25.0	$\uparrow T_{film,max}^{des}$
7°	10	51.2	90	2	944	51.2	94.2	48.2	6.6	622.7	41	6.9	25.7	↓*Lifetime*
8°	8	39.5	100	2	1335	48.6	95.6	46.5	15.6	625.8	32	5.9	26.3	↓*Lifetime*
–	8	26.7	140	$\uparrow \Delta p_{rec}^{des}$ regardless the offset + ↓*Lifetime* with offset above 2										
–	8	51.2	70	↓*Lifetime* regardless the offset + $\uparrow T_{film,max}^{des}$ with offset above 3										
–	10	26.7	170	$\uparrow \Delta p_{rec}^{des}$ regardless the offset										
–	12	26.7	210	$\uparrow \Delta p_{rec}^{des}$ regardless the offset										

Table 5
Main characteristics of the cylindrical, optimized star and Gemasolar-like star receivers.

Item	Unit	Cylindrical	Gemasolar-like Star	Optimized Star (740H)	Optimized Star (H230)	Optimized Star (800H)
Field		Gemasolar-like		Surrounded		
Receiver material		H230	H230	740H	H230	800H
Receiver height (H_{rec})	[m]	16.0	16.0	10.0	10.0	12.0
Receiver diameter (D_{rec})	[m]	8.0	8.7	10.4	10.4	12.0
N° of panels (N_p)	[−]	16	12 (5–5-2)	12 (5–5-2)	12 (5–5-2)	12 (5–5-2)
Tubes per ray (N_{tr})	[−]	–	100	120	120	140
Tubes per panel (N_{tp})	[−]	38	20–20-50	24–24-60	24–24-60	28–28-70
Number of total tubes (N_t)	[−]	608	300	360	360	360
Tube external diameter ($D_{ext,t}$)	[mm]	39.5	39.5	39.5	39.5	39.5
Tube thickness	[mm]	1.65	1.65	1.65	1.65	1.65

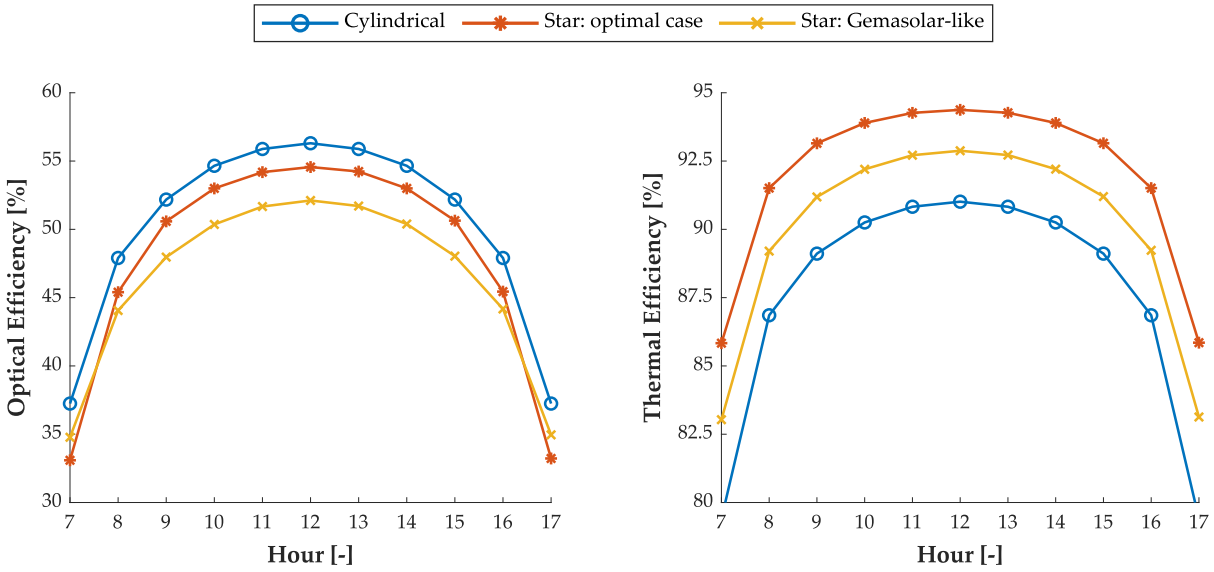

Fig. 10. Optical and thermal efficiencies trend during the investigated day for cylindrical, Gemasolar-like star and optimized star configurations (Haynes 230).

23.2 €/MWh and is obtained with a receiver height of 12 m and 140 tubes per ray having an outer diameter of 39.5 mm. When 740H or H230 are considered as tubes material the optimized configuration has $H_{rec} =$ 10 m and $D_{ext,t} = 39.5$ mm showing LCOH of 26.1 €/MWh and 27.2 €/MWh, respectively, about 12 % and 17 % higher compared to 800H. For all materials the configurations with 26.7 mm tubes were rejected due to too high receiver pressure drop. It is important to notice that all the investigated configurations comply with the resistance criterion for the wind load verification.

Another interesting result is the optimized maximum heat flux that reaches value of 1528 kW/m^2 with 740H, followed by 1159 kW/m^2 with H230 and 1072 kW/m^2 with 800H. This points out how the star-shaped configuration allows to exceed the typical limit of 1000 kW/m^2 of state-of-the-art cylindrical receivers[15].

5.2. Comparison with cylindrical receiver

In this section the optimized star-shaped receivers obtained in the previous section are compared with the state-of-the-art external cylindrical receiver of the Gemasolar power plant based in terms of performance, costs, and LCOH. For this analysis, the star receiver is coupled with its preferable surrounded field (Fig. 8b) while the cylindrical one is analyzed considering the Gemasolar-like solar field shown in Fig. 8a. However, limiting the comparison to these two cases would entail a not fair analysis, as an optimized receiver (i.e. star, designed to minimize the LCOH in the previous section) would be compared with a non-optimized one (i.e. cylindrical, whose characteristics are taken from references). Therefore, an additional case is investigated, in which the Gemasolar-like solar field is equipped with a non-optimized star receiver, having same height and tube dimensions and comparable diameter of Gemasolar's cylindrical receiver (namely, "Gemasolar-like Star"). Haynes230 is assumed as tubes material for the Gemasolar-like cylindrical and star receivers [46] while all the three investigated materials are considered for the optimized star configurations. The main characteristics of the five compared cases are reported in Table 5.

In Fig. 10 daily optical, thermal and solar-to-thermal efficiencies are depicted, together with a bar plot showing all the different losses. The optimized star receiver case represented in the Figure has H230 as tubes material.

Fig. 10 shows that, if the star receiver is not optimized (Gemasolar-like star case), it has lower solar-to-thermal efficiency than the cylindrical one. This is mainly due to the lower optical efficiency caused by the higher spillage losses which outweigh lower reflective and thermal losses. When the optimized star configuration coupled with the surrounded field is considered, the optical efficiency is still lower than the cylindrical receiver one, but significantly higher than the Gemasolar-like star case thanks to the solar field best suited to the star geometry and the larger diameter of the receiver. In addition, the significantly higher thermal efficiency leads to a solar-to-thermal efficiency slightly higher than the cylindrical case. Summarizing, Fig. 11 shows that the

[15] The case with 740H, $H_{rec} = 10$ m and $D_{ext,t} = 39.5$ mm was not simulated with offset values greater than 11 despite the non-achievement of any constraint and the continuous decrease of LCOH, as the results show the achievement of a plateau as the offset varies. In fact, already from offsets greater than 9 the change in LCOH, film temperature, pressure drop and lifetime as offset increases becomes negligible.

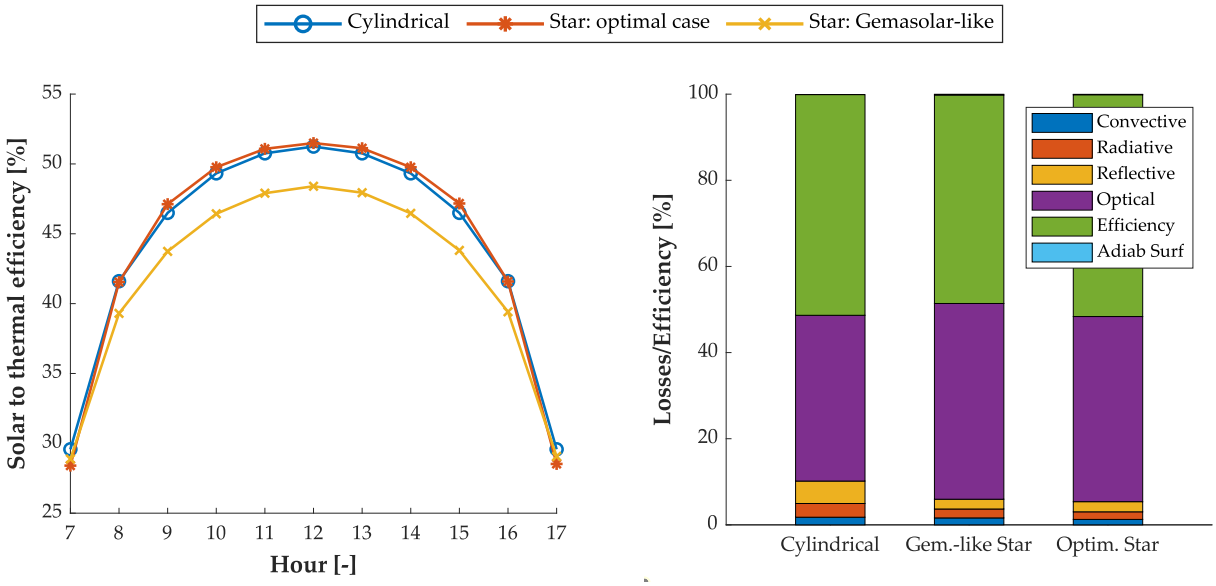

Fig. 11. Solar-to-thermal efficiency during the investigated day (left) and thermal losses items (right) for the cylindrical, Gemasolar-like star and optimized star configurations (Haynes 230). In the losses comparison plot "Adiab Surf" indicates the radiative power hitting the external supports of each ray.

Table 6
Energy performance and costs of the cylindrical, optimized star and Gemasolar-like star receivers.

Item	Unit	Cylindrical	Gemasolar-like Star	Optimized Star (H230)	Optimized star (740H)	Optimized star (800H)
Design optical efficiency (η_{opt}^{des})	[%]	56.3	52.1	54.6	56.6	57.4
Design thermal efficiency (η_{th}^{des})	[%]	91	93.1	94.5	94.7	93.3
Design solar-to-thermal efficiency (η_{stt}^{des})	[%]	51.2	48.5	51.6	53.6	53.5
Design maximum heat flux (q''_{max})	[kW/m^2]	986	865	1159	1528	982
Design receiver pressure drop (Δp_{rec}^{des})	[bar]	8	18	14	15	12
Design maximum film temp. ($T_{film,max}^{des}$)	[°C]	595	606	631	644	642
Creep-fatigue lifetime	[years]	49	193	90	58	42
Manufacturing and installation costs:						
- tubes	[M€]	28.7	14.1	10.6	10.3	3.5
- headers	[M€]	1.1	0.5	0.6	0.6	0.2
- manifolds	[M€]	0.9	1.1	1.4	1.3	0.4
- coating	[M€]	0.2	0.2	0.1	0.1	0.2
Receiver engineering cost ($C_{rec,eng}$)	[M€]	3.9	3.9	3.9	3.9	3.9
Receiver cost (C_{rec})	[M€]	34.7	19.7	16.6	16.2	8.1
Capital Expenditure (CAPEX)	[M€]	120.5	102.3	98.9	98.4	88.5
Operating Expenses (OPEX)	[M€/year]	1.7	1.4	1.4	1.4	1.2
Yearly thermal energy production ($\dot{Q}_{HTF}^{y}$)	[GWh/year]	275.3	260.0	275.6	285.9	288.6
Levelized Cost of Heat (LCOH)	[€/MWh]	33.2	29.9	27.2	26.1	23.2

star receiver, when properly designed and coupled with a suitable solar field, has energy performance comparable to, and even slightly better than, conventional cylindrical receivers. What the figure does not show, however, is that for the same solar field and thermal input on the receiver, the star configuration has i) about half the tubes (300 against 608) that leads to a receiver cost reduction by 43 % and ii) a significantly longer lifetime that would make it possible to use less performing and cheaper materials (such as 800H) with a further reduction in CAPEX. These aspects are highlighted by Table 6, that shows design energy performance, capital and operating costs, and LCOH of the five investigated cases, obtained applying the methodology outlined in Section 2 to the case study described in Section 4.

As it can be noticed, already the replacement of the cylindrical receiver with the Gemasolar-like star configuration leads to a reduction in LCOH by about 10 % (from 33.2 €/MWh to 29.9 €/MWh). As anticipated, this is primarily driven by the lower number of tubes in the star configuration, which allows for a significant reduction in CAPEX, outweighing the decrease in yearly energy performance[16].

When also the solar field is replaced to make it more suitable to the star configuration, and the receiver design is optimized through the methodology presented in this study, receiver construction costs can be reduced to less than one-fourth, leading to a 30 % lower LCOH. Moreover, the table highlights the remarkably higher mechanical resistance of star-shaped receivers over cylindrical ones. Indeed, while the cylindrical receiver has an estimated lifetime of 49 years, the Gemasolar-like star receiver, despite requiring roughly half of the tubes of the cylindrical, shows a lifetime of 193 years. Such a long lifetime would allow replacing the material with less expansive alternatives or reduce the receiver size further limiting its cost. This result is aligned with the outcome of the study from Binder et al. [15] that showed the

[16] Provided by the metal cost multiplied by the correction factor defined in Section 2.6.

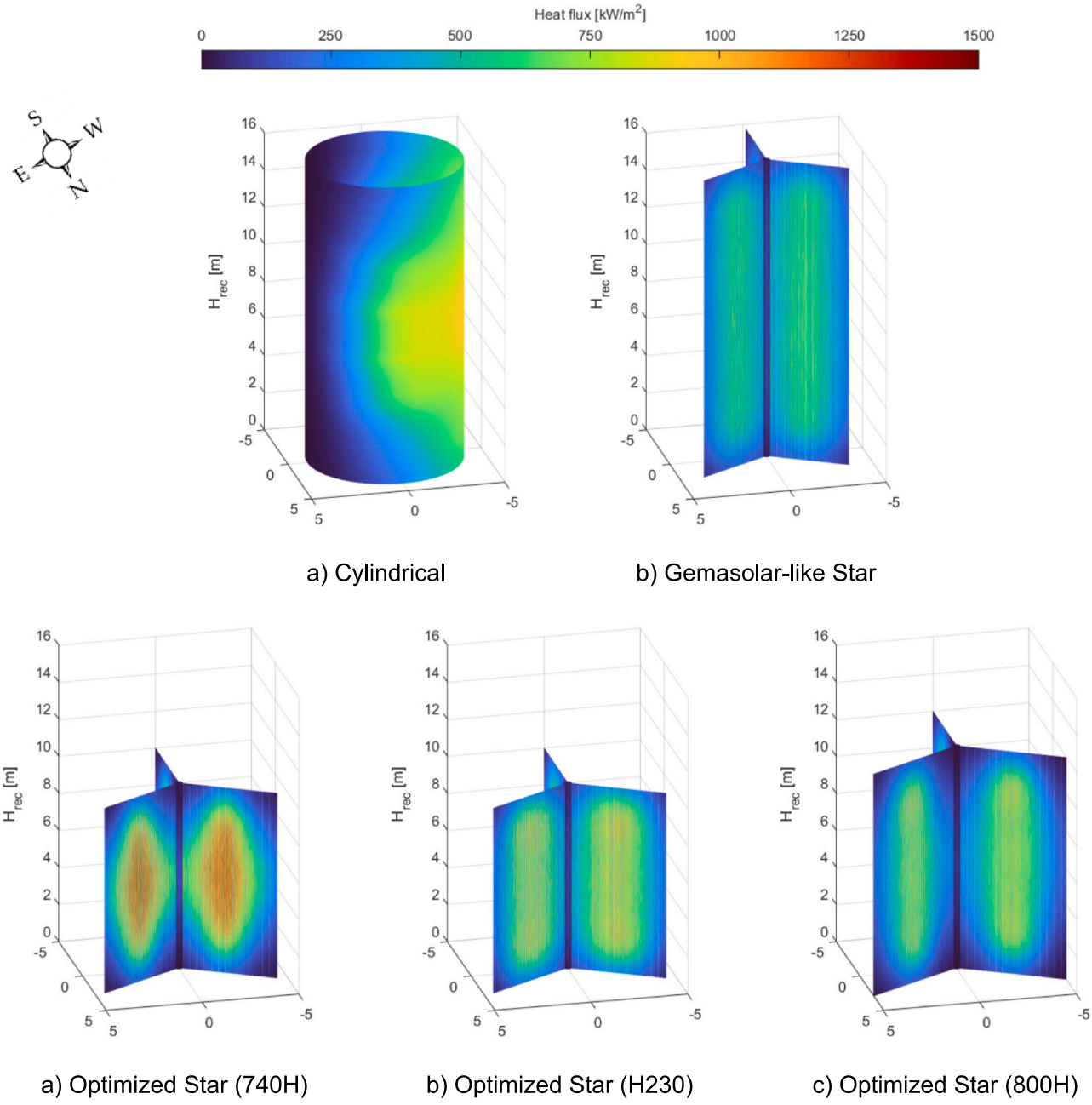

Fig. 12. Design heat flux map on the optimized receivers.

significantly higher lifetime of double-sided irradiated tubes over one-side irradiated ones.

Moreover, it is interesting to notice how the HTF pressure drop are generally higher in the star configurations with respect to the cylindrical one, due to the different hydraulic configuration and the mixing of the HTF before entering the third ray of the star-shaped receiver. Despite the higher pressure drop, which results in higher thermal energy wasted to feed the pumps, star-shaped receivers have better overall energy performance, with the optimized configuration collecting around 5 % more thermal energy in one year (288.6 GWh/year against 273.5 GWh/year).

The design heat flux maps on the five receivers are shown in Fig. 12. The figure confirms that moving from conventional cylindrical to star-shaped receivers allows to remarkably increase, for a given material, the maximum heat flux on the receiver. In fact, the external receiver with a maximum heat flux of 986 kW/m^2 has a lifetime of 49 years, and thus with limited space for increasing the heat flux further, while the optimized star receiver with the same material (H230) shows a peak heat flux of 1159 kW/m^2 with a lifetime of 90 years.

6. Conclusions

The article describes a comprehensive methodology to i) assess the maximum size of star-shaped receivers that can withstand the wind load for a specific location, ii) optimize the design of star receivers minimizing the Levelized Cost of Heat while making sure that constrains on wind load resistance, pressure drop, film temperature, and creep-fatigue lifetime are met, and iii) compare performance and costs of star receivers to state-of-the-art external cylindrical receivers.

Firstly, a simplified one-dimensional model based on the EUROCODE standard and on the principle of virtual works, was implemented to estimate the maximum size, in terms of rated thermal input, that a star-shaped receiver can reach withstanding the wind load for given location

and geometrical characteristics.

Results of the model application showed that star receivers can be adopted for middle-large scale plants if designed with adequate materials and geometrical characteristics.

Then, a comprehensive modelling framework was implemented to perform a techno-economic optimization of the star receiver design, for a given solar field and location. The method is based on a parametric approach and uses the LCOH as Key Performance Indicator to identify the optimized receiver configuration. In detail, optical analysis was performed using ray-tracing simulation tools while tailored numerical models were implemented in MATLAB to investigate thermal, mechanical and economic aspects. Constraints on wind load resistance, receiver pressure drop, maximum film temperature and creep-fatigue lifetime were introduced to guarantee the component structural integrity.

The optimization methodology was applied to design a star-shaped receiver operating in a solar tower plant similar to the Gemasolar Thermosolar Plant, operating in Sevilla since May 2011. Results showed that the lowest LCOH is 23.2 €/MWh and is obtained with a receiver height of 12 m and 140 tubes per ray having an outer diameter of 39.5 mm and manufactured with Incoloy 800H.

Lastly, star-shaped receiver was compared from a techno-economic perspective to the state-of-the-art cylindrical receiver and the outcome pointed out that replacing a Gemasolar-like cylindrical receiver with a star receiver having the same height and external diameter as well as the same design thermal power, leads to a reduction in LCOH by about 10 %. When the heliostats field is tailored on the star-shaped geometry through a more “surrounded” design, and the receiver is optimized through the methodology presented in the article, its construction costs can be reduced to less than one-fourth if compared to the cylindrical configuration, leading to a 30 % lower LCOH. If compared to the cylindrical case, the optimized star configuration has higher design optical efficiency, thermal efficiency and HTF pressure drop; results of the simplified yearly analysis pointed out that this configuration collects around 5 % more thermal energy in one year.

The results highlight the significant impact that this innovative receiver configuration can have in making for Concentrated Solar Power plants based on the central tower concept more techno-economically attractive and competitive with other renewable technologies.

Future studies may focus on the development of tailored methodologies to optimize the heliostats position and aiming points in case of star-shaped configurations, or on more detailed analysis of the wind load on star receivers, perhaps based on three-dimensional finite elements methods. In addition, further research works may include the application of the proposed methodology for star receivers design optimization with a finer discretization of the investigated design parameters (i.e., receiver height and tubes diameter) or analyzing also the impact of other important parameters such as the receiver aspect ratio, the number of rays or the number of panels per ray. Lastly, a thorough investigation of the detailed engineering design aspects of this innovative receiver concept is essential for appropriately sizing and positioning the various components (e.g., nozzles, welded supports, headers, manifolds, etc.).

CRediT authorship contribution statement

Giancarlo Gentile: Writing – original draft, Visualization, Software, Methodology, Investigation, Data curation, Conceptualization. **Francesco Stefano Carli:** Visualization, Software, Methodology, Investigation, Data curation. **Matteo Speranzella:** Visualization, Software, Methodology, Investigation, Data curation. **Marco Binotti:** Writing – review & editing, Methodology, Conceptualization. **Michael E. Cholette:** Writing – review & editing, Methodology, Conceptualization. **Giampaolo Manzolini:** Writing – review & editing, Supervision, Resources, Methodology, Conceptualization.

Declaration of competing interest

The authors declare that they have no known competing financial interests or personal relationships that could have appeared to influence the work reported in this paper.

Data availability

Data will be made available on request.

References

[1] Merchán RP, Santos MJ, Medina A, Calvo Hernández A. High temperature central tower plants for concentrated solar power: 2021 overview. Renew Sust Energ Rev 2022;155:111828. https://doi.org/10.1016/J.RSER.2021.111828.
[2] International Energy Agency. Technology roadmap solar thermal electricity: Technical report. 52; 2014.
[3] U.S. Department of Energy. SunShot Vision Study. 2012.
[4] Turchi CS, Heath GA. Molten Salt Power Tower Cost Model for the System Advisor Model (SAM) 2013. https://doi.org/10.2172/1067902.
[5] National Renewable Energy Laboratory (NREL). System Advisor Model (SAM). https://sam.nrel.gov/; 2025. accessed October 10, 2024.
[6] Zavoico AB. Solar power tower design basis document. 2001.
[7] González-Gómez PA, Rodríguez-Sánchez MR, Laporte-Azcué M, Santana D. Calculating molten-salt central-receiver lifetime under creep-fatigue damage. Sol Energy 2021;213:180–97. https://doi.org/10.1016/J.SOLENER.2020.11.033.
[8] Kelly BD. Advanced thermal storage for central receivers with supercritical coolants. 2010.
[9] Ho CK, Christian JM, Ortega JD, Yellowhair J, Mosquera MJ, Andraka CE. Reduction of radiative heat losses for solar thermal receivers. In: Plesniak AP, Pfefferkorn C, editors. High Low Conc. Syst. Sol. Energy Appl. IX. 9175. SPIE; 2014. p. 917506. https://doi.org/10.1117/12.2063152.
[10] Christian JM, Ortega JD, Ho CK. Novel Tubular Receiver Panel Configurations for Increased Efficiency of High-Temperature Solar Receivers. ASME 2015 9th Int Conf energy sustain ES 2015, collocated with ASME 2015 power Conf ASME 2015. 13th Int Conf fuel cell Sci Eng Technol ASME 2015 Nucl forum 2015;1. https://doi.org/10.1115/ES2015-49431.
[11] Christian JM, Ho CK, Ortega JD, Yellowhair J. Design and Modeling of Light-Trapping Tubular Receiver Panels. ASME 2016 10th Int Conf energy sustain ES 2016, collocated with ASME 2016 power Conf ASME 2016. 14th Int Conf fuel cell Sci Eng Technol 2016;1. https://doi.org/10.1115/ES2016-59158.
[12] Puppe M, Giuliano S, Frantz C, Uhlig R, Flesch R, Schumacher R, et al. Techno-economic optimization of molten salt solar tower plants. AIP Conf Proc 2018;2033:40033. https://doi.org/10.1063/1.5067069/1023223.
[13] Wang WQ, Qiu Y, Li MJ, Cao F, Bin Liu Z. Optical efficiency improvement of solar power tower by employing and optimizing novel fin-like receivers. Energy Convers Manag 2019;184:219–34. https://doi.org/10.1016/J.ENCONMAN.2018.12.029.
[14] Wang WQ, Qiu Y, Li MJ, He YL, Cheng ZD. Coupled optical and thermal performance of a fin-like molten salt receiver for the next-generation solar power tower. Appl Energy 2020;272:115079. https://doi.org/10.1016/J.APENERGY.2020.115079.
[15] Binder M, Schloms F, Kuhl M, Schuhbauer C, Uhlig R, Schwarzbözl P, et al. Design study for the lifetime of double-sided irradiated absorber tubes. Sol Energy 2022;248:16–27. https://doi.org/10.1016/J.SOLENER.2022.10.059.
[16] EN 1991-1-4:2005 Eurocode 1: Actions on structures - Part 1–4: General actions - Wind actions. 2005.
[17] ASME. ASME boiler and pressure vessel code 2007, sec 2-materials, part D-properties (metric). American Society of Mechanical Engineers; 2007.
[18] Wagner MJ, Wendelin T. SolarPILOT: a power tower solar field layout and characterization tool. Sol Energy 2018:171. https://doi.org/10.1016/j.solener.2018.06.063.
[19] Wendelin T, Dobos A, Lewandowski A. SolTrace: A Ray-Tracing Code for Complex Solar Optical Systems 2013. https://doi.org/10.2172/1260924.
[20] Wagner MJ, Wendelin T. SolarPILOT: a power tower solar field layout and characterization tool. Sol Energy 2018;171:185–96. https://doi.org/10.1016/J.SOLENER.2018.06.063.
[21] Gentile G, Picotti G, Binotti M, Cholette ME, Manzolini G. Dynamic thermal analysis and creep-fatigue lifetime assessment of solar tower external receivers. Sol Energy 2022;247:408–31. https://doi.org/10.1016/J.SOLENER.2022.10.010.
[22] Gentile G, Picotti G, Binotti M, Cholette ME, Manzolini G. A comprehensive methodology for the design of solar tower external receivers. Renew Sust Energ Rev 2024;193:114153. https://doi.org/10.1016/J.RSER.2023.114153.
[23] Gentile G, Picotti G, Casella F, Binotti M, Cholette ME, Manzolini G. SolarReceiver2D: a Modelica package for dynamic thermal modelling of central receiver systems. IFAC-PapersOnLine 2022;55:259–64. https://doi.org/10.1016/j.ifacol.2022.09.105.
[24] Anderson CB, Gentile G, Longhi A, Casella F, Cholette M, Manzolini G. Advanced Controllers for Heat Transfer Fluid Mass Flow Rate Control in Solar Tower Receivers. Proc 29th Sol Paces Conf 2023 2024:1–9. https://doi.org/10.52825/solarpaces.v2i.913.
[25] Hottel HC, Sarofim AF. Radiative transfer15; 1967. https://doi.org/10.1002/aic.690150504.

[26] Lauzier N. View factors. MATLAB Cent File Exch. https://it.mathworks.com/matlabcentral/fileexchange/5664-view-factors; 2021.
[27] Levin SR. Collision of incompressible fluid flows in pipelines. Trans LTI Im SM Kirova 1958;8:89–93.
[28] Gentile G, Picotti G, Binotti M, Cholette ME, Steinberg TA, Manzolini G. A methodology for the creep-fatigue analysis of external receivers for solar tower plants using real weather data. AIP Conf Proc 2023:2815. https://doi.org/10.1063/5.0150847.
[29] Logie WR, Pye JD, Coventry J. Thermoelastic stress in concentrating solar receiver tubes: a retrospect on stress analysis methodology, and comparison of salt and sodium. Sol Energy 2018;160:368–79. https://doi.org/10.1016/J.SOLENER.2017.12.003.
[30] Neises TW, Wagner MJ, Gray AK. Structural Design Considerations for Tubular Power Tower Receivers Operating at 650°C. ASME 2014 8th Int Conf energy sustain ES 2014 collocated with ASME 2014. 12th Int Conf fuel cell Sci Eng Technol 2014;1. https://doi.org/10.1115/ES2014-6603.
[31] Bree J. Elastic-plastic behaviour of thin tubes subjected to internal pressure and intermittent high-heat fluxes with application to fast-nuclear-reactor fuel elements. J Strain Anal 1967;2:226–38. https://doi.org/10.1243/03093247v023226.
[32] American Society of Mechanical Engineers (ASME). ASME Boiler and Pressure Vessel Code, 1980 Code Cases: Nuclear Components Code Case N-47. 1980.
[33] Turchi CS, Boyd M, Kesseli D, Kurup P, Mehos MS, Neises TW, et al. CSP Systems Analysis - Final Project Report 2019. https://doi.org/10.2172/1513197.
[34] Ho CK, Pacheco JE. Levelized cost of coating (LCOC) for selective absorber materials. Sol Energy 2014;108:315–21. https://doi.org/10.1016/J.SOLENER.2014.05.017.
[35] Maxwell C. Cost indices. https://www.toweringskills.com/financial-analysis/cost-indices/; 2022.
[36] Laporte-Azcué M, González-Gómez PA, Rodríguez-Sánchez MR, Santana D. Material selection for solar central receiver tubes. Sol Energy Mater Sol Cells 2021;231:111317. https://doi.org/10.1016/j.solmat.2021.111317.
[37] Laporte-Azcué M, González-Gómez PA, Rodríguez-Sánchez MR, Santana D. Material selection for solar central receiver tubes. Sol Energy Mater Sol Cells 2021;231:111317. https://doi.org/10.1016/J.SOLMAT.2021.111317.
[38] Rinaldi F, Binotti M, Giostri A, Manzolini G. Comparison of linear and point focus collectors in solar power plants. Energy Procedia 2014;49:1491–500. https://doi.org/10.1016/J.EGYPRO.2014.03.158.
[39] Binotti M, Astolfi M, Campanari S, Manzolini G, Silva P. Preliminary assessment of sCO2 cycles for power generation in CSP solar tower plants. Appl Energy 2017;204:1007–17. https://doi.org/10.1016/J.APENERGY.2017.05.121.
[40] Pipe Size Chart - Rolled Alloys. https://www.rolledalloys.com/pipe-chart/; 2025. accessed November 22, 2023.
[41] SolarReserve. Crescent Dunes Solar Energy Plant 2014. http://website.eventpower.com/paperclip/exhibitor_docs/15AE/SolarReserve_311.pdf (accessed January 18, 2022).
[42] Montoya A, Rodríguez-Sánchez MR, López-Puente J, Santana D. Numerical model of solar external receiver tubes: influence of mechanical boundary conditions and temperature variation in thermoelastic stresses. Sol Energy 2018;174:912–22. https://doi.org/10.1016/J.SOLENER.2018.09.068.
[43] EnergyPlus. https://energyplus.net/; 2025. accessed November 25, 2023.
[44] Manzolini G, Binotti M, Bonalumi D, Invernizzi C, Iora P. CO2 mixtures as innovative working fluid in power cycles applied to solar plants. Techno-economic assessment Sol Energy 2019;181:530–44. https://doi.org/10.1016/j.solener.2019.01.015.
[45] McMurtrey MD, Rupp RE, Barua B, Messner MC. Creep-fatigue behavior and damage accumulation of a candidate structural material for concentrating solar power thermal receiver - quarter 6 report. Idaho Natl Lab; 2019.
[46] Laporte-Azcué M, González-Gómez PA, Rodríguez-Sánchez MR, Santana D. A procedure to predict solar receiver damage during transient conditions. Renew Sust Energ Rev 2022;154:111905. https://doi.org/10.1016/J.RSER.2021.111905.
[47] Cammalleri M, Costanza A. A closed-form solution for natural frequencies of thin-walled cylinders with clamped edges. Int J Mech Sci 2016;110:116–26. https://doi.org/10.1016/j.ijmecsci.2016.03.005.